

REPUBLIC OF TURKIYE
AYDIN ADNAN MENDERES UNIVERSITY
GRADUATE SCHOOL OF NATURAL AND APPLIED SCIENCES
HEAD OF DEPARTMENT OF MECHANICAL ENGINEERING
MASTER'S PROGRAM

**DESIGN AND OPTIMIZATION OF PROPELLER OF
SUBMERSIBLE MIXER FOR BIOGAS PLANTS**

UTKU KÖSE
MASTER'S THESIS

SUPERVISOR
Prof. Dr. İSMAİL BÖĞREKÇİ

AYDIN-2023

ACCEPTANCE AND APPROVAL

The thesis titled “DESIGN AND OPTIMIZATION OF PROPELLER OF SUBMERSIBLE MIXER FOR BIOGAS PLANTS”, prepared by Utku KÖSE, a student of Department of Mechanical Engineering Program at T.C. Aydın Adnan Menderes University, Graduate School of Natural And Applied Science, was accepted as a Master's Thesis by the jury below.

Date of Thesis Defence: 03/08/2023

Member (T.D.)	: Prof. Dr. İsmail. BÖĞREKÇİ	Aydın Adnan Menderes University
Member	: Prof. Dr. Pınar DEMİRCİOĞLU	Aydın Adnan Menderes University
Member	: Assoc. Prof. Dr. Arzum İŞİTAN	Pamukkale University

APPROVAL:

This thesis was approved by the jury above in accordance with the relevant articles of the Aydın Adnan Menderes University Graduate Education and Examination Regulations and was approved on the by from the Board of Directors of the Graduate School of Science in the..... numbered decision.

Prof. Dr. Mustafa SÜR MEN

Institute Director

ACKNOWLEDGEMENTS

I would like to thank my advisor, Prof. Dr. İSMAİL BÖĞREKÇİ, who showed his trust in me throughout my thesis and took a close interest in my work. I would like to convey my endless respects to my esteemed teacher Prof. Dr. PINAR DEMİRCİOĞLU, who guided me with his advice and spared time for me in my studies.

I am grateful to my friend ENGİN ORÇUN KOZAKA, who gave me the opportunity to work physically and technically during the thesis work, for his trust and patience in me.

I would like to express my endless thanks to my close friends and family who always motivate me.

TABLE OF CONTENTS

ACKNOWLEDGEMENTS	iii
LIST OF SYMBOLS AND ABBREVAITONS.....	v
ÖZET.....	xi
ABSTRACT	xii
1. INTRODUCTION.....	1
2. LITERATURE REVIEW.....	4
3. MATERIAL AND METHOD	7
3.2.1. Pitch.....	8
3.2.1.1.Skew	10
3.2.1.2.Blade Profile Section Geometry and Definition	12
3.3. Governing Equations.....	17
3.4. Pre-Processing.....	18
3.4.1. Meshing	22
3.4.2. Simulation Model & Boundary Conditions	23
3.5. Running Simulations.....	26
4. RESULTS	28
4.1. Sample Simulation Results	29
4.2. Sensitivity Results.....	33
5. DISCUSSION	37
6. CONCLUSION AND RECOMMENDATIONS.....	40
REFERENCES.....	42
APPENDIX.....	45
SCIENTIFIC ETHICS STATEMENT.....	50
CURRICULUM VITAE.....	51

LIST OF SYMBOLS AND ABBREVAITIONS

BGP	: Biogas Plant
MW	: Megawatt
Kw	: Kilowatt
h	: Hour
c_p	: Non-Dimensionalized Camber Position
c_m	: Non-Dimensionalized Camber Position With Blade Width
ANSYS	: Engineering Simulation Software
NACA	: National Advisory Committee For Aeronautics
NURBS	: Non-Uniform Rational Basis Spline
AS	: Active Subspaces
RANS	: Reynolds Averaged Navier-Stokes
k	: Turbulent Kinetic Energy
ε	: The Strain Rate Tensor
ω	: Dissipation Rate
τ	: The Stress Tensor
SST	: Shear Stress Transport
SVL	: Sound Pressure Level
DTMB 4119	: David Taylor Model Basin Type Propeller
J	: Advance Ratio
BEM	: Blade Element Momentum
DO	: Dynamic Optimization
PBCF	: Propeller Boss Cap Fins
ISO	: International Organization for Standardization
CMM	: Coordinate Measuring Machine
CAESES	: CAE (Computer-Aided Engineering) System Empowering Simulation
α	: Pitch Angle
P	: Pitch Distance

π	: Pi Number
arctan	: The Inverse of The Tangent Function
D	: Propeller Diameter
R	: Propeller Radius
R	: Radius of A Propeller Section
P	: Nondimensional Radius
θ	: Pitch Angle
Θ_s	: Skew Angle of A Propeller Section
Θ_{sp}	: Skew Angle of Propeller
S	: The Skew
Cos	: Cosine
NASA	: National Aeronautics And Space Administration
∇	: Nabla
P	: Density of The Fluid
V	: Velocity Vector
T	: Dimensionless Curve Parameter
P	: Pressure
τ	: Stress Tensor
F	: Body Force
μ	: Dynamic Viscosity
ε	: Strain Rate
λ	: Second Viscosity Coefficient
I	: Identity Matrix.
T	: Transpose of A Matrix
y^+	: Y Plus
Re	: Reynolds Number
ρ	: Density
V	: Velocity
L	: Characteristic Length Scale of The Flow
u^*	: Shear Velocity

T_w	: Wall Shear Stress
N	: Kinematic Viscosity of The Fluid
U_R, U_T, U_A	: Velocity Components (Radial, Tangential And Axial)
N	: Newton
C	: Chord Length
G	: Gravity
$\bar{\sigma}_t$: Mean Velocity
$\bar{\sigma}_t$: Mean Shear Stress



LIST OF FIGURES

Figure 3.1: The propeller pitch P is the theoretical linear distance a propeller travels during a complete rotation (Njaastad et al., 2022).	9
Figure 3.2: Definition of pitch [1] helix definition on a cylinder of Radius r (Charlton, 2018).	9
Figure 3.3 Reference frames: (a) global reference frame and (b) local reference frame (Charlton, 2018).	10
Figure 3.4: Skew Definition (Charlton, 2018).	11
Figure 3.5: The difference between aft- and forward skew, with the blade reference line marked (Njaastad et al., 2022).....	12
Figure 3.6: General definition of an aerofoil section (Charlton, 2018).....	13
Figure 3.7: Input table of blade section profile script	14
Figure 3.8: Example blade section creation parameters.....	14
Figure 3.9: Blade section profile	14
Figure 3.10: Example blade section creation parameters.....	15
Figure 3.11: Input parameters depending on the propeller diameter (Parameter distributions)	15
Figure 3.12: Blade section profile	16
Figure 3.13: Blade profile distribution.....	16
Figure 3.14: Propeller solid model (a) Propeller Front view (b) Propeller top view	19
Figure 3.15: 3D Flow field boundary and stator and rotor regions (a) Flow field boundaries and surface mesh. (b) Rotational region. (c) Propeller surface mesh.	20
Figure 3.16: General representation of flow domain and details of computational mesh. (a) General domain section @ $x = 0$. (b) Mesh detail inside the rotational region. (c) prism cells around Blade hub inside the boundary layer.	21
Figure 3.17: Calculation Area and Boundary Conditions	24
Figure 3.18: Optimization flowchart	27
Figure 4.1: Streamlines	29
Figure 4.2: Pressure distribution in cylindrical section.....	30
Figure 4.3: Speed profiles under flow. (a) Axial Speeds. (b) Radial Speeds. (c) Tangential speeds	31

Figure 4.4: Pressure coefficient distributions in 4 radial sections of 4 different designs. (a) $r/R = 0.2$ (b) $r/R = 0.4$, (c) $r/R = 0.6$, (d) $r/R = 0.8$ 33

Figure 4.5: DK75 Design set results 34

Figure 4.6: DK110 Design set results. 35

Figure 4.7: DK150 Design set results. 35

Figure 5.1: The Results of the Sensitivity Analysis in CAESES 39



LIST OF TABLES

Table 1: The Boundary Conditions for Pressure, Velocity, Turbulent Kinetic Energy and Omega	24
Table 2: Design parameters, limit points and number of selected points.....	28
Table 3: Design Results Thurst, Moment, Power, Thurst/Power.....	36



ÖZET

BİYOĞAZ TESİSLERİNDE KULLANILAN DALGIÇ KARIŞTIRICILARIN PERVANE TASARIMI VE OPTİMİZASYONU

Köse U. Aydın Adnan Menderes Üniversitesi, Fen Bilimleri Enstitüsü, Makine Mühendisliği Programı, Yüksek Lisans Tezi, Aydın, 2023.

Amaç: Bu tez çalışmasında, biyogaz santrali fermentörlerinde kullanılan eksenel karıştırıcıların bilgisayar destekli mühendislik hesaplama araçları kullanılarak hidrolik tasarımlarının yapılması, küçük ölçekli modeller ile havuz testlerinin yapılması ve son olarak prototiplerinin üretilmesi amaçlanmıştır.

Materyal ve Yöntem: Bu tez çalışmasında tasarım ve optimizasyon için bilgisayar destekli mühendislik araçları kullanılarak konvansiyonel eksenel biyogaz karıştırıcı verimliliğinin iyileştirilmesi planlanmıştır. Bu amaca, performans metriklerini (yani güç, tork, itme) ölçmek için açık kaynaklı bir CFD analiz yazılımı OpenFOAM ile birlikte kanat geometrisi için parametrik bir tasarım kullanılmıştır.

Bulgular: En verimli tasarım ile itme-güç oranını en üst düzeye çıkararak, oldukça büyük bir parametrik durum uzayı oluşturulmuştur. Bu uzayda ikamet eden bir dizi tasarım adayı arasından dört farklı tasarıma ulaşılmıştır. Bu tasarımlar karşılaştırılarak dizayn parametrelerinin sonuçlara etkileri değerlendirilmiştir.

Sonuç: Bu çalışmada hassasiyet sonuçları karşılaştırıldığında, kanat verimliliğine en çok etki eden faktörlerin çarpıklık ve hatve olduğu saptanmıştır.

Anahtar Kelimeler: Dalgıç karıştırıcı, pervane, parametrik tasarım, OPEN FOAM, gübre

ABSTRACT

DESIGN AND OPTIMIZATION OF PROPELLER OF SUBMERSIBLE MIXER FOR BIOGAS PLANTS

Köse U. Aydın Adnan Menderes University, Graduate School of Natural and Applied Sciences, Mechanical Engineering Program, Master Thesis, Aydın, 2023.

Objective: In this thesis, it is aimed to make hydraulic designs of axial mixers used in biogas plant fermenters using computer aided engineering calculation tools, to make pool tests with small scale models and finally to produce prototypes.

Material and Methods: In this thesis, it is planned to improve the efficiency of the conventional axial biogas mixer by using computer aided engineering tools for design and optimization. To this end, a parametric design for blade geometry was used in conjunction with an open source CFD analysis software OpenFOAM to measure performance metrics (i.e. power, torque, thrust).

Results: By maximizing the thrust-to-power ratio with the most efficient design, a fairly large parametric state space is created. Four different designs were reached from a series of design candidates residing in this space. By comparing these designs, the effects of design parameters on the results were evaluated.

Conclusion: When the sensitivity results were compared in this study, it was determined that the factors affecting the blade efficiency the most were skew and pitch.

Keywords: submersible mixer, propeller, parametric design, Open FOAM, Manure

1. INTRODUCTION

In recent years, about 90% of the world's primary energy demand has been met from fossil fuels such as coal, crude oil and natural gas. In the future, the utilization of fossil fuel reserves and their negative effects on the environment require the utilization of renewable energy sources (Ohnmacht et al., 2021). In that sense, the rate of technological development and active redesign of renewable energy plants, their sub-components and processes are important. Biogas production and utilization have shown a steady rising trend in recent years. Due to the presence of significant numbers of biogas producers and sellers of plant components in the market, there is a strong demand that is constantly increasing. The so-called anaerobic process of decomposing organic mass by depriving it of oxygen produces a gas mixture called biogas. Biogas can be used directly as a multifunctional energy source such as heating and lighting, as well as converting it into other types of energy such as mechanical and electrical energy. Energy is obtained by burning directly from biogas, which has a high energy value. It can be used as fuel in internal combustion engines and can directly generate mechanical work or electricity.

Expansion of biogas production and utilization has shown a very strong development over the past years. Strong demand, which has been steadily increasing due to the significant number of biogas producers and plant components vendors have established themselves in the market. Biogas is produced during anaerobic degradation of organic matter in different environments such as landfills and biological waste digesters. Methane, used as biofuel for heat and electricity generation, is the main component of biogas and is not only a valuable source of renewable energy, but also a harmful greenhouse gas emitted into the atmosphere (Rasi et al., 2021). The biogas generation process is a biochemical process. It consists of four stages: hydrolysis, acidification, acetone production, and methane production. In this process, it is obtained efficiently with the harmony of microbial flora and mechanical design.

Mixing of non-Newtonian fluid flows is used in many applications, especially in the process industry, but also in wastewater treatment or biogas power plants. According to Moeller and Torres (1997) study, the wastewater sludge does not behave like a Newtonian fluid, but it behaves such a pseudo plastic fluid. On the other side, Slurries are generally non-Newtonian fluids (Moeller et al., 1997). Studies on power consumption have shown the importance of the mixers used in increasing process efficiency. In Germany, until the end of the 2012, about 7589

BGP have processed with approximately 3719 MW electrical capacity. The calculations show that 1 billion kW h/a were used for agitation in Germany Biogas Station, if it is considered that the approximately 8% of produced electricity was used for BGP operations and 50% of these energies were spend for agitation (Moeller et al., 1997; Naegele et al., 2012). Approximately 200 million €/a was used for agitations at a cost of energy of 0.2 €/kW h. This calculation is clearly demonstrating that the effects of agitations on the profitableness of BGP working (Lemmer et al., 2013). While vertically aligned mixers are preferred in the process industry, wastewater treatment and biogas plants often use mixers with horizontally aligned shafts (i.e. axial mixer) (Reviol et al., 2018). Submersible mixers are 1 vital wastewater treatment machines widely used in urban and rural wastewater treatment farms. Submersible mixers are used in biochemical reactions such as anaerobic digestion, sedimentation, wastewater aeration and more (Błoński et al., 2021). The main tasks of mixing are to distribute the newly added substrates inside the reactor, release the produced biogas from digestion to the gas tank, smooth out the disruptive temperature and concentration gradients, and in particular prevent both sinking and floating layers (Karim et al., 2005; Kress et al., 2018).

The use of propeller mixers is particularly important for applications with high flow rates (Zlokarnik, 1999). Propeller mixers are usually centrally arranged, but an eccentric location is also possible. They belong to the category of axial fluid machines and are used for turbulent and high viscous fluid flow. It reaches the typical viscosity value, but propeller agitators also agitate fluids of approximately higher viscosity (Zlokarnik, 1999; Reviol et al., 2018). Agitators with propellers are mostly used in the field of wastewater treatment and biogas power plant technology.

Propeller designs are critical in submersible mixer operation. The power consumption of the mixers used is important for the efficiency of the mixer. However, power consumption is also related to the waste heat generation of the electric motor, and therefore a poorly designed propeller can cause overheating when operating at off design conditions and therefore complete disruption to the mixing process may occur (Reviol et al., 2018).

The submersible pump is a series connection of stages consisting of an impeller and a diffuser (Stel et al., 2015). The impellers connected to a single shaft all rotate at the same angular velocity. Although the impellers rotate at a constant angular velocity throughout the pump, the flow structure in each stage differs greatly from the other stages (Li et al., 2016). These differences lead to the formation of a complex flow structure and thus cause great difficulties in the experimental characterization of the flow field through the pump. Another

difficulty in experimental characterization is that the measured values can vary dramatically depending on many parameters such as fluid viscosity-temperature, impeller vane inlet-outlet angle, diffuser vane inlet-outlet angle, vane number, inter-stage distance, surface roughness and so on. The general trend nowadays is to address the above-mentioned problems experimentally. numerical simulations validated with data. This trend has recently in parallel with the development of numerical solution methods in the years, computer capacities is a result of the significant progress achieved.

The study experimentally investigated the effect of intermediate vanes on pump performance in a submersible pump (Golcu et al., 2006). They conducted their research by considering a total of 12 different configurations of pump impellers with different number of vanes and intermediate vane sizes. As a result of their research, they found that the application of intermediate vanes will provide a limited improvement in pump performance in certain configurations. The study investigated the optimum vane structure for a centrifugal pump using orthogonal experimental and numerical methods (Zhou et al., 2013). In their research, they designed and modeled 16 different impeller structures using orthogonal table. The study numerically investigated pressure fluctuations as a result of the interaction between the pressure field across the rotating impeller and the pressure field across the fixed diffuser (Berten et al., 2007). The simulations were carried out using the 3DRANS CFD-code (CFX 10). The study aims to develop a methodology for the prediction of hydroacoustic pressure fluctuations caused by rotor-stator interaction in centrifugal pumps. In this study, the optimum design parameters for a diffuser are numerically investigated (Zhou et al., 2012). In their research, they used the ANSYS-Fluent package program to solve the Navier Stokes Equations in the numerical simulation process. They performed the simulations considering two different diffusers and selected the pressure conversion parameter as the evaluation parameter. In this study, the steady and unsteady radial forces along the pump are investigated experimentally and numerically. The experimental measurements were carried out by means of a pressure scanner and numerical simulations were carried out with the ANSYS-Fluent package program. The research was carried out within the scope of impellers with two different outlet diameters in the same volume.

2. LITERATURE REVIEW

Lemmer et al. (2013) measured the efficiency in two different mixing systems. Nutrient distributions in digesters of renewable energy crops and animal manures were measured by taking different samples with a newly developed probe immersed in concrete roofs at different heights and sections of the digester. Significant local variations in the concentration of organic acids were detected in different agitator types and regimes, and at the same time, it was observed that the low speed mixer with large diameter propeller provided an improvement of 70% compared to the small diameter and high speed mixer in the instantaneous measurements in electrical energy measurements.

Mola et al. (2019) is a multidisciplinary study for the determination of the wing shape to reduce the vortex-induced pressure and increase the efficiency without making any changes on the thrust. The propeller blades are parameterized as NACA blades or with a precise shape of NURBS curves constructed with specific points as a function of chord, pitch, skew and rake distribution. The shapes obtained as a result of the created control points are fully automated according to the variables. The created geometries are used for potential flow solution in a software based on Boundary Element Method. First, a linear combination of the entire original geometry for a precise approach is proposed based on a single relative variable, and then the data from potential flow simulations are used to implement a parameter space reduction method based on active subspaces (AS). As a final step, some selected blade shapes were analyzed with high-accuracy RANS simulation and the optimum shape was determined accordingly.

Belhenniche et al. (2016) based on the Seiun Maru propeller geometry, which is basically the shape on which the propeller shapes are based, analyzes were made in the form of steady and transient but non-uniform ship wave using 14 different propeller configurations and standard $k-\varepsilon$ and $k-\omega$ SST models. Thrust, torque and efficiency coefficients obtained from numerical simulations were compared with experimental data. Standard $k-\varepsilon$ and $k-\omega$ SST models are guaranteed for suitability in open flow conditions. As a result of the parametric study, the optimum parameters of the shape providing the best hydrodynamic performance were obtained. Another conclusion of the study is that a lower expanded ratio wing design is required for best efficiency. Another determination made is that even-numbered propellers work more noiselessly than odd numbered ones.

Gorji et al. (2017) carried out a study that allows making hydro-acoustic predictions with the help of RANS solver at different skew and rake angles. These angles, which cause pressure fluctuations and consequently propeller noise, are calculated using the two-step Ffows Williams and Hawkings equations to calculate the hydrodynamic pressure. In addition, with the help of the same equation, numerical solutions were obtained at different points of the sound pressure level (SVL) propels. The DTMB 4119 propeller was chosen for analysis due to its large experimental data pool. It has been observed that the hydrodynamic characteristics under different operating conditions are in good agreement with the experimental data. While the efficiency was low under heavy working conditions, the efficiency increased in light working conditions. The pressure distribution is also drawn at $(r/R) = 0.7$ and $J = 0.83$, which expresses the ratio of the local radius point to the total radius, and is in agreement with the experimental data. As a result, it has been determined that the propellers skew and rake angles have a noise effect.

Mahmuddin, (2017) developed a computational method based on Blade Element Momentum (BEM) theory to optimize and analyze blades for an optimal exploration and improvement of wind energy. This developed method has been compared with another BEM software, QBlade, which is highly accepted. By plotting the axial and angular induction factors for varying radial positions, very small differences were detected between the BEM and the QBlade, especially at high speeds. The reason for this difference is that the extrapolation developed by BEM and QBlade software for lift and drag data is different. In addition, depending on the wind speed, it was seen that both software were very similar in strength.

Doijode et al. (2022) created 3 different design sets to optimize the propellers and used a machine learning approach to solve the changes in these design sets. For the first set of designs, performance evaluation was taken into account, and high efficiency and low cavitation were taken into account in this regard. For the second set of designs, low efficiency and high cavitation are taken into account without considering performance. In the third case, which is the last design set, BEM was used. The purpose of such a broad clustering is to teach clusters a wide range for multi-objective optimization. Classical characteristics of a blade such as chordlength, pitch, skew, rake, thickness distribution are not used because of their multi-dependency, instead a new completely independent parametric model is proposed with parameters directly obtained from the propeller blade mesh. Blade surface mesh parameters, which are in good agreement with the CFD and BEM performance estimations, are more advantageous than the classical variables in this case. With several BEM evaluations, a well-

performing design set was created. In this study, Wageningen B-4 70 propellers were used because it has the data to verify and validate the results. As a result, Dynamic Optimization (DO) is more efficient in generating utility clusters than conventional design parameters.

Yin et al. (2023), studies were conducted on the optimum design of a Propeller Boss Cap Fins to improve energy efficiency. First, it started from an original design of a Ro-Ro ship with a modern four-wing and no PBCF because it had experimental data in its original design. Then, CFD analyzes of the design with PBCFs were made by reducing the size to find the optimum design. The 10 most suitable shapes were selected for optimization and then the most optimum design was obtained for the propeller/rudder. In the design point study, the new PCBFs achieved a 1.043% efficiency gain over the original design. This increase in efficiency is due to the hub vortex and, in part, to produce more thrust. On the other hand, yield strength analysis showed that optimum designs of PCBFs did not undergo any structural deformation when operating under normal load conditions.

Njaastad et al. (2022), a new method has been developed to determine the design parameters of propeller blades belonging to an ISO 484 class. This method, which can be used in the accuracy of manufactured blades such as reverse engineering and wear evaluation of a propeller, retrieves data from a set of scanned points. This method, which involved determining a camber line based on Voronoi Digrams and Delaunay Triangulation, was applied to a blade of KKVLC2 propels and compared to CMM measurements. As a result, different geometric design parameters can be determined by this method.

3. MATERIAL AND METHOD

In order to carry out optimization studies, the blade geometry should be linked to quantitative variables. For this purpose, in the literature review, ship propellers and axial pumps were examined and the general variables required to form the blade form were found the blade geometry sketch was created using the CAESES program according to the input parameters

In order to complete the optimization cycle, it is necessary to find the thrust that the blade geometry will create in the flow and the torque values that will be needed to obtain this thrust. For this purpose, simulations have been made using the OpenFOAM software package and it has been shown that the outputs corresponding to the input values (thrust, power and the ratio of thrust force to power) can be calculated. After showing that the relationship between input and output variables can be found with the help of CFD simulations, these simulations were added to the optimization study. Optimization process proceeds in two stages. In the first stage, sensitivity analysis and state space are created between the lower and upper limits of the input variables. In the second stage, optimization work is carried out on the created state space.

As the starting point of the designs, the needs of the working environment were taken into consideration. These mixers will generally operate in an environment where mainly water and slurry are present. It has been determined that in cases where the material is slurry, it will work at low Reynolds numbers due to the rheological properties of the slurry. In line with these findings, the optimum airfoil [blade/propeller] to operate at low and high Reynolds numbers was investigated and optimized.

In the following sections, information is given about how the blade geometry is created and how it is parameterized, how simulations are made and optimization studies.

3.1.Preparing a Parametric Blade Geometry

3.2. Blade and Blade Section Forms

We can collect the parameters that will form the blade geometry under two main headings. Variables that change along the blade radius and the variables that define the airfoil obtained at a constant radius.

- Blade Variables
 - Pitch
 - Skew
- Blade Profile Section Geometry and Definition
 - Blade Thickness
 - Blade Camber
 - Blade Chord Length

3.2.1. Pitch

The propeller pitch is the theoretical distance P_a propeller will move forward in a solid medium for each rotation, not allowing for slip. The distance is illustrated in Figure 3.1. The pitch of a blade section can also be defined as an angle. The relation between the pitch distance P and the pitch angle α is given by

$$\alpha = \arctan(P/2\pi r) \quad (1)$$

Typically, the propeller blades are twisted to achieve almost constant pitch of the blades from root to tip. To describe this twist, a pitch distribution $P(r)$ is given, where r is the Radius considered. The relationship between pitch angle and pitch distribution can then be expressed as

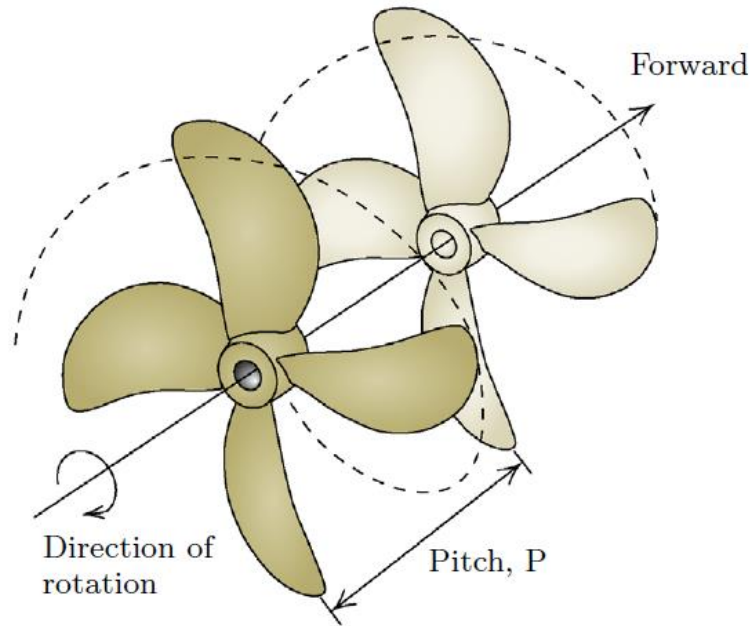


Figure 3.1: The propeller pitch P is the theoretical linear distance a propeller travels during a complete rotation (Njaastad et al., 2022).

$$\alpha = \arctan (P(r)/2\pi r) = \arctan(P(\rho)2\pi \rho R) \quad (2)$$

where $R = D/2$ is the propeller radius and ρ is the nondimensional radius defined by

$$\rho = r/R \quad (3)$$

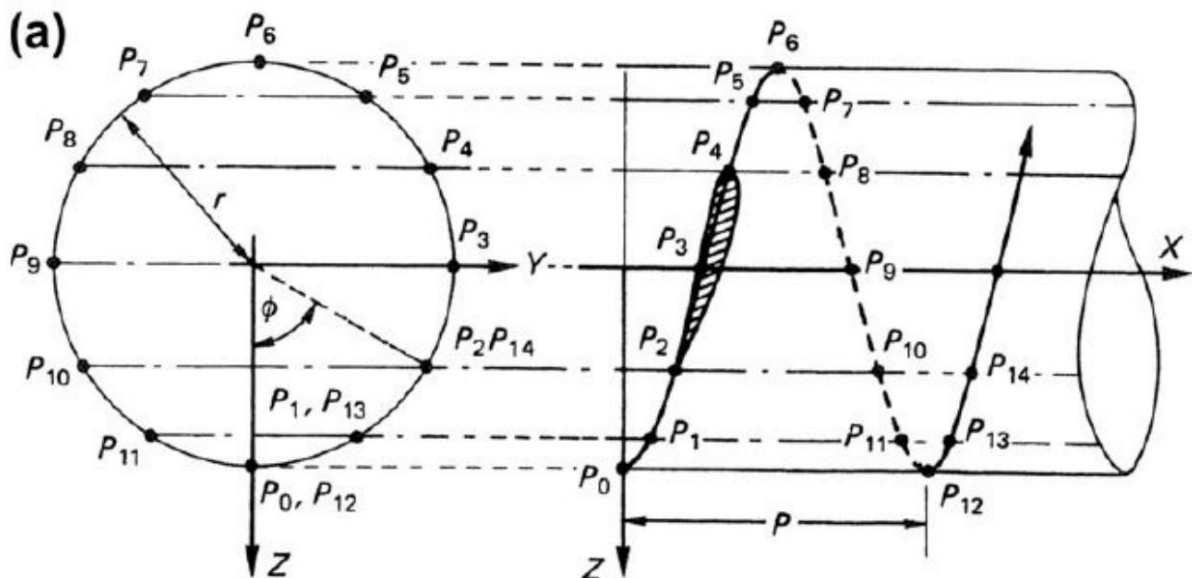


Figure 3.2: Definition of pitch [1] helix definition on a cylinder of Radius r (Charlton, 2018).

Or we can explain the pitch angle, P0 to P12 as shown Figure 3.2, assuming the distance traveled along the X axis as P, the pitch angle is calculated as in equation 4.

$$\theta = \tan^{-1} (P/2\pi r) \tag{4}$$

3.2.1.1. Skew

The skew angle $\Theta_s(x)$ of a particular section, Figure 3.4, is the angle between the directrix and a line drawn through the shaft center line and the mid-chord point of a section at its non-dimensional radius (x) in the projected propeller outline; that is, looking normally, along the shaft center line, into the y-z-plane of Figure 3.3. Angles forward of the directrix, which is in the direction of rotation, in the projected outline are considered to be negative.

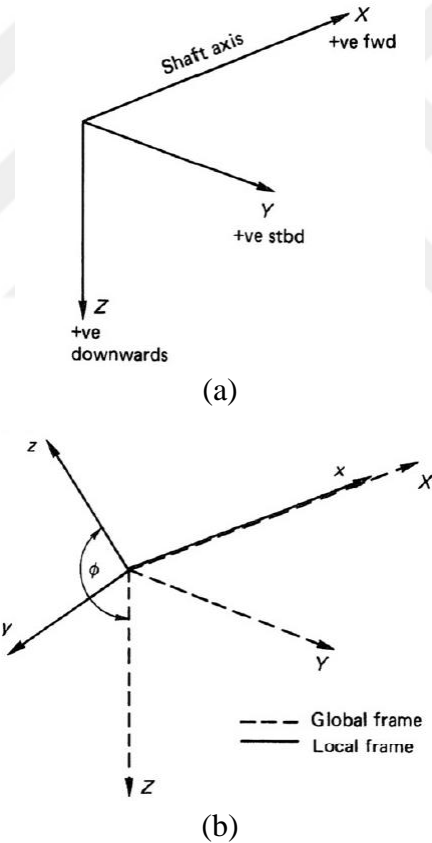


Figure 3.3 Reference frames: (a) global reference frame and (b) local reference frame (Charlton, 2018).

The propeller skew angle (Θ_{sp}) is defined as the greatest angle, measured at the shaft center line, in the projected plane, which can be drawn between lines passing from the shaft center line through the mid-chord position of any two sections.

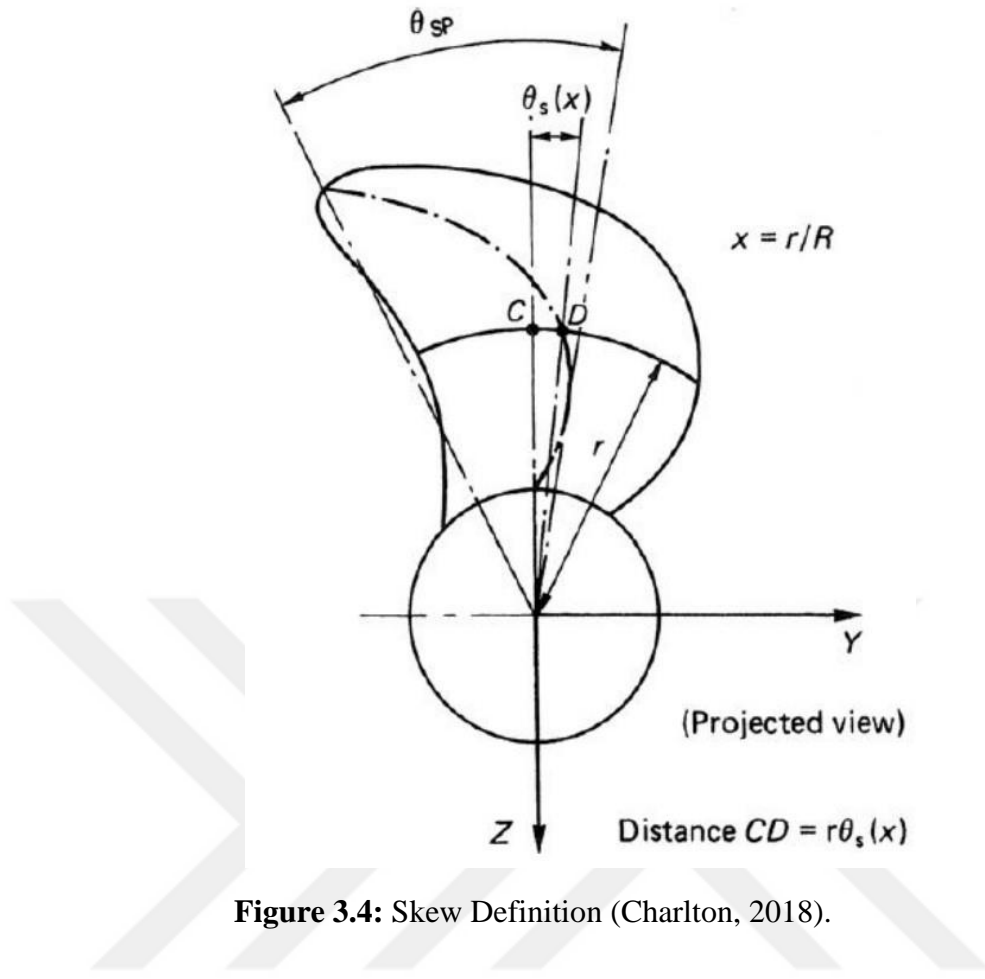


Figure 3.4: Skew Definition (Charlton, 2018).

The skew angle $\Theta_s(r)$ of a particular section is the tangential component of the angle formed on the propeller blade between the propeller reference line (z-axis) and a radial line from the propeller origin, passing through the mid-chord of the considered section at radius r . The purpose of a skewed shape is to avoid cavitation while maintaining propeller efficiency (Charlton, 2018).

The propeller skew angle Θ_{sp} is the largest spanning angle between two lines from the propeller origin running through the various mid-chords of the radial blade sections.

For a given foil section at radius r , the skew can be expressed as

$$S = r \Theta_s(r) / \cos(\alpha) \tag{5}$$

Where $\Theta_s(r)$ is the skew angle, and α is the pitch angle for the considered foil section. The propeller skew can be divided into forward and aft skew. A propeller for which the blades

are swept in the direction of rotation is said to have forward skew. An aft skewed propeller has blades swept opposite of the direction of rotation. These concepts are illustrated in Figure 3.5.

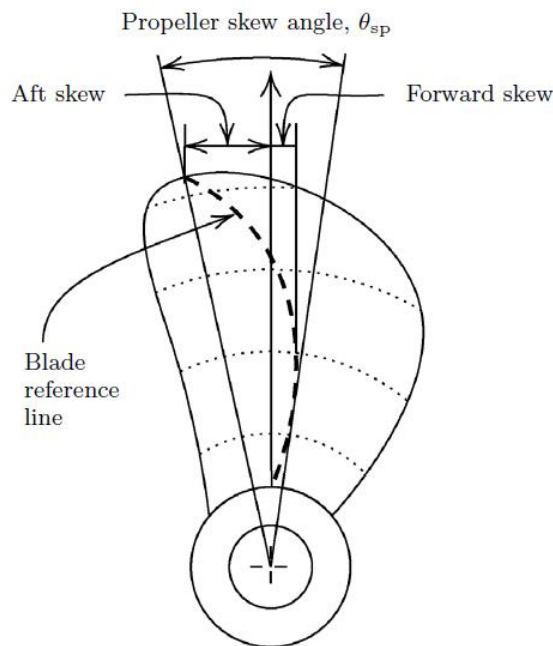


Figure 3.5: The difference between aft- and forward skew, with the blade reference line marked (Njaastad et al., 2022).

3.2.1.2. Blade Profile Section Geometry and Definition

In the early 1930s the National Advisory Committee for Aeronautics (NACA) in the USA now known as NASA embarked on a series of aerofoil experiments which were based on aerofoil geometry developed in a rational and systematic way. Some of these aerofoil shapes have been adopted for the design of marine propellers, and as such have become widely used by manufacturers all over the world. Consequently, this discussion of aerofoil geometry will take as its basis the NACA definitions while at the same time recognizing that with the advent of prescribed velocity distribution capabilities some designers are starting to generate their own section forms to meet specific surface pressure requirements.

Figure 3.6 shows the general definition of the aerofoil. The mean line or camber line is the locus of the mid-points between the upper and lower surfaces when measured perpendicular to the camber line. The extremities of the camber line are termed the leading and trailing edges of the aerofoil and the straight line joining these two points is termed the chord line. The

distance between the leading and trailing edges when measured along the chord line is termed the chord length (c) of the section. The camber of the section is the maximum distance between the mean camber line and the chord line, measured perpendicular to the chord line.

The aerofoil thickness is the distance between the upper and lower surfaces of the section, usually measured perpendicularly to the chord line although strictly this should be to the camber line. The leading edges are usually circular, having a leading-edge radius defined about a point on the camber line (Charlton, 2018).

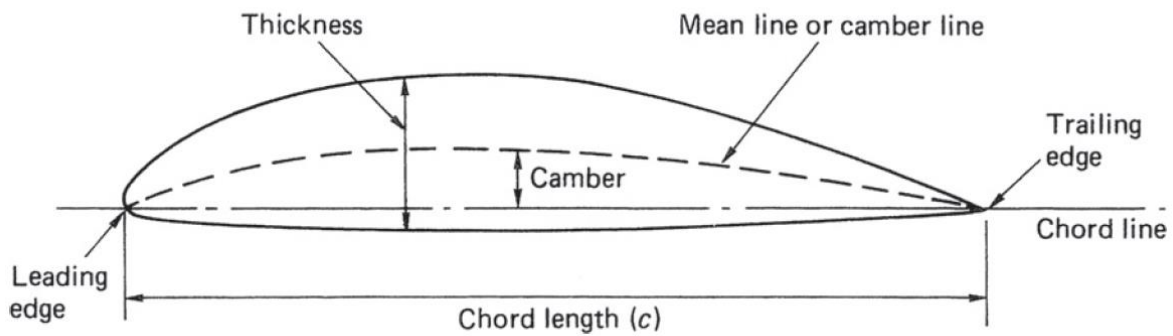


Figure 3.6: General definition of an aerofoil section (Charlton, 2018).

The sections of the blade form, whose general definition is given above, are formed with the NACA-4 camber equation, constant thickness and circular leading and trailing edges. The camber airfoil is defined by the equations 6, 7 and 8 given below. In these equations, t is the dimensionless curve parameter ranging from 0 to 1, c_p is the nondimensionalized [dimensionless] position with the blade width where the camber gets the greatest value, and c_m is the dimensionless size of the camber again with the blade width.

$$x = t \tag{6}$$

$$t < c_p \rightarrow y = c_m * \frac{2c_p t - t^2}{c_p^2} \tag{7}$$

$$t > c_p \rightarrow y = c_m * \frac{1 - 2 * c_p + 2 * c_p * t - t^2}{1 - c_p^2} \tag{8}$$

The script prepared with the help of the equations given above is given in Appendix 1.

	Type	Name	Default Value	Allow Expression	Required	Category	Label	Advanced	
1	FDouble	chord	1	X	X		Genislik	Edit	+
2	FDouble	camberpos	0.4	X	X		Kamber Pozisyonu	Edit	+
3	FDouble	camber	0.02	X	X		Kamber Büyüklüğü	Edit	+
4	FDouble	thickness	0.08	X	X		Kalınlik	Edit	+

Figure 3.7: Input table of blade section profile script

The screenshot where this script is defined and input values are selected is shown in Figure 3.7.

The screenshot shows a software interface for defining blade section parameters. At the top, there is a text input field containing 'f1'. Below it is a 'General' tab with a right-pointing arrow. Under the 'General' tab, there are four parameter fields, each with a dropdown arrow and a help icon (question mark):

- Genislik: 1
- Kamber Pozisyonu: 0.4
- Kamber Büyüklüğü: 0.02
- Kalınlık: 0.02

Figure 3.8: Example blade section creation parameters



Figure 3.9: Blade section profile

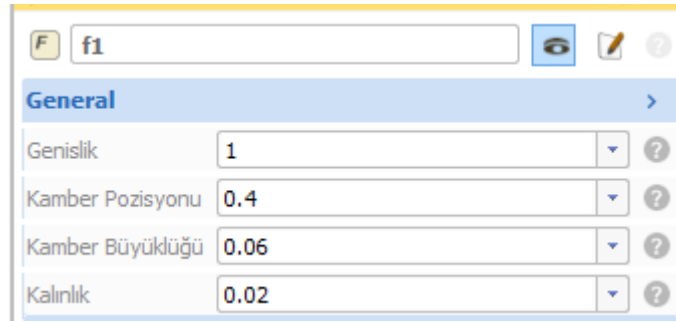


Figure 3.10: Example blade section creation parameters

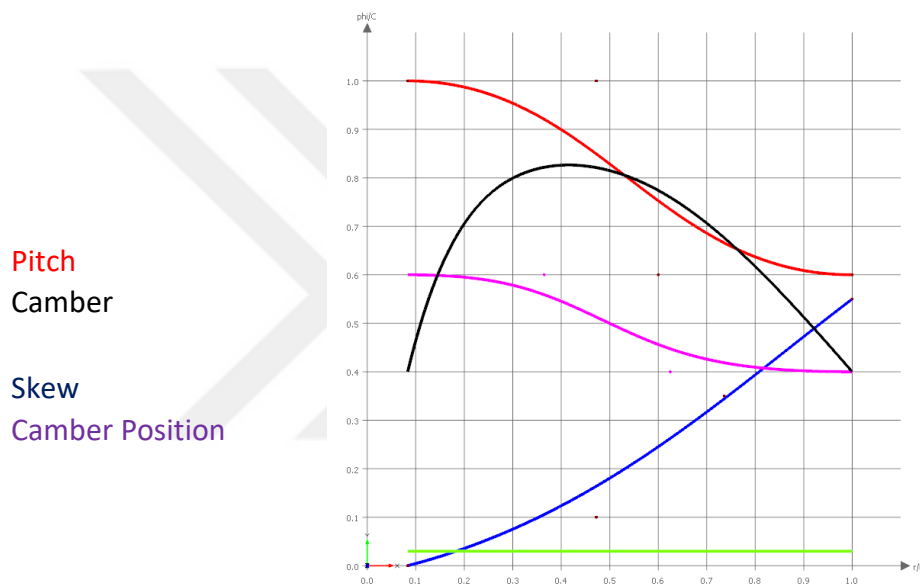


Figure 3.11: Input parameters depending on the propeller diameter (Parameter distributions)



Figure 3.12: Blade section profile

Figure 3.9 and Figure 3.12 shows two different blade section profiles Figure 3.8 and Figure 3.10, respectively. It shows how it was created using the inputs.

Sections created according to the radial distribution functions given in Figure 3.11 are shown in Figure 3.13 and 3D views of the propeller are shown in Figure 3.14

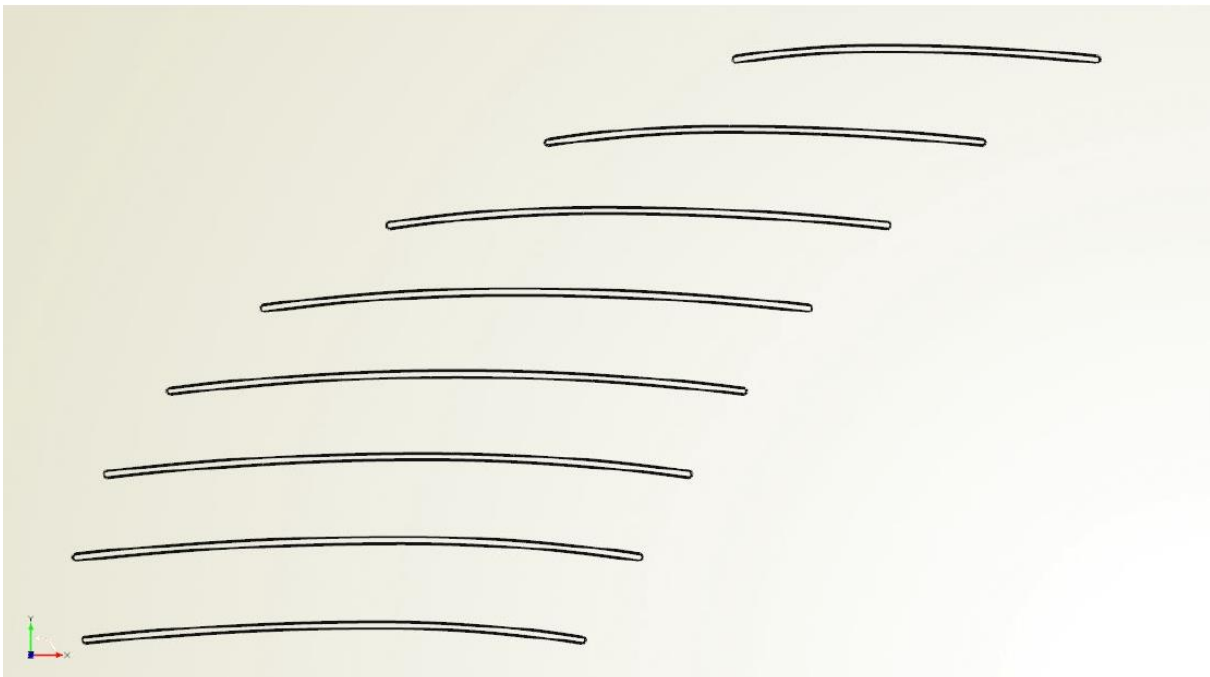


Figure 3.13: Blade profile distribution

3.3. Governing Equations

The governing equations for the flow around a propeller of a submersible mixer in a biogas plant can be described using the Navier-Stokes equations. The Navier-Stokes equations are a set of differential equations that govern the motion of fluid in three dimensions, and they describe how the velocity, pressure, temperature, and density of a fluid vary over time and space. In general, the Navier-Stokes equations are very difficult to solve analytically, and numerical techniques are typically used to solve them. Since the working fluid is in liquid phase incompressible assumption can be made and the incompressible Navier-Stokes equations can be expressed as:

Continuity Equation:

$$\nabla \cdot \mathbf{V} = 0 \quad (9)$$

Momentum Equation:

$$\rho (\partial \mathbf{V} / \partial t + \mathbf{V} \cdot \nabla \mathbf{V}) = -\nabla p + \nabla \cdot \boldsymbol{\tau} + \mathbf{F} \quad (10)$$

where: ρ is the density of the fluid, \mathbf{V} is the velocity vector, t is time, p is the pressure, $\boldsymbol{\tau}$ is the stress tensor, \mathbf{F} is the body force, such as gravity.

The continuity equation represents the conservation of mass and states that the rate of change of mass in a fluid element is equal to the net mass flux into or out of the element. The momentum equation represents the conservation of momentum and states that the rate of change of momentum in a fluid element is equal to the sum of the forces acting on the element.

The stress tensor, $\boldsymbol{\tau}$, is given by:

$$\boldsymbol{\tau} = 2\mu\boldsymbol{\varepsilon} + \lambda\nabla \cdot \mathbf{V}\mathbf{I} \quad (11)$$

where: μ is the dynamic viscosity of the fluid, $\boldsymbol{\varepsilon}$ is the strain rate tensor, which describes the deformation of the fluid, λ is the second viscosity coefficient, and \mathbf{I} is the identity matrix.

The strain rate tensor, $\boldsymbol{\varepsilon}$, is given by:

$$\boldsymbol{\varepsilon} = 0.5(\nabla \mathbf{V} + (\nabla \mathbf{V})^T) \quad (12)$$

where T denotes the transpose of a matrix.

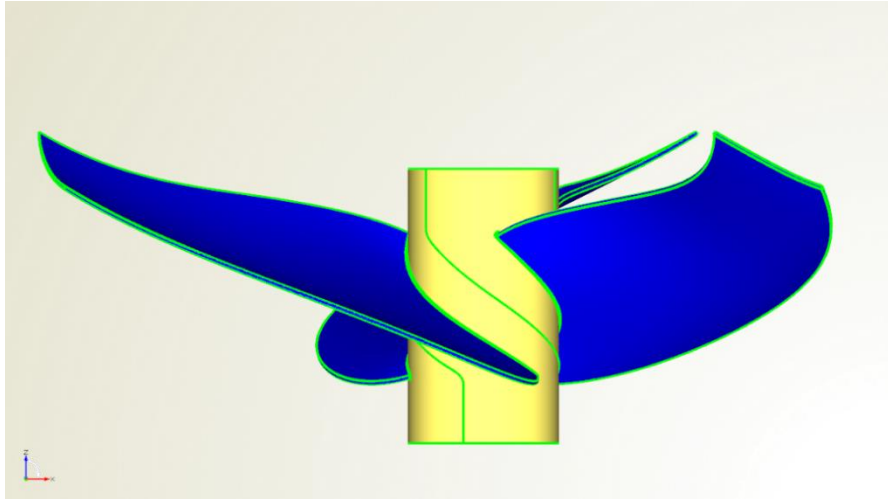
In order to solve the Navier-Stokes equations numerically, a computational fluid dynamics (CFD) approach can be used. This involves discretizing the governing equations using a numerical method such as finite difference, finite volume or finite element methods, and solving the resulting set of algebraic equations on a discretized mesh. The resulting solution provides detailed information about the flow field, including velocity, pressure, and can be used to optimize the design of the propeller for maximum mixing efficiency and minimum energy consumption.

3.4.Pre-Processing

The first step in preprocessing is transferring the propeller geometry to the mesh generation software in .step format. While creating the propeller geometry, it has been observed that primary and secondary type discontinuities on surfaces defined as boundary representations create problems when defining the computational mesh (especially if the boundary curves used in surface definition are splitted). As a solution, a filleting operation between the hub and the blade, prevents the formation of splitted boundary curves.



(a)



(b)

Figure 3.14: Propeller solid model (a) Propeller Front view (b) Propeller top view

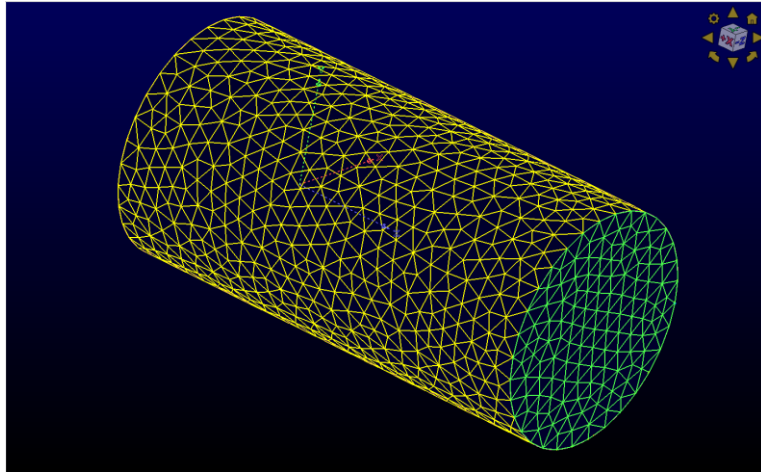
In this way, all curves that make up the blade structure are extracted fully automatically in the mesh creation script prepared. The steps of the script are importing the geometry, determining the edge curves and surfaces, generating an initial surface mesh on the propeller and the boundary surfaces, creating the 3D volumetric mesh in rotor and stator regions, and finally exporting the mesh in OpenFOAM format. The mesh consists of tetrahedral cells and contains regular hexahedral cells in the boundary layer in accordance with the requirements of the turbulence model (the distance of the first grid cell on the wall to the wall is between $y^+ = 30-50$). y^+ is a non-dimensional number which signifies the ratio between the viscous length scale to physical length scales. When the modelling conditions are satisfied, the total number of computational cells become approximately 8 million. In

Figure 3.15 (a) general of the flow domain can be seen.

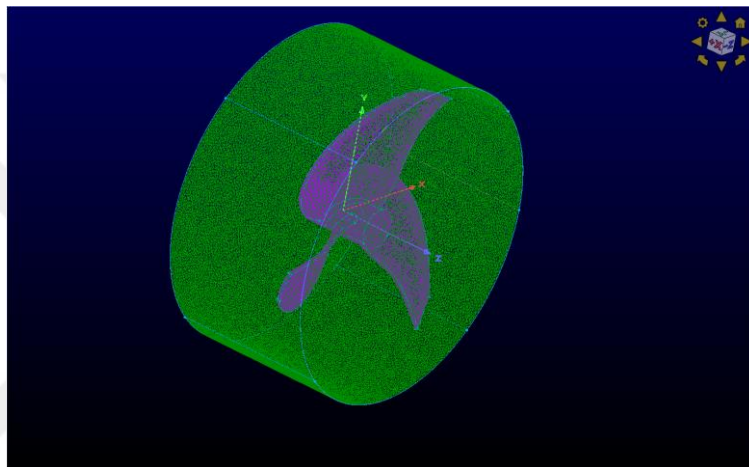
Figure 3.15 (a) shows the stationary part of the computational domain together with the boundaries.

Figure 3.15 (b) shows the rotational part of the computational domain and the AMI (arbitrary mesh interface) surfaces.

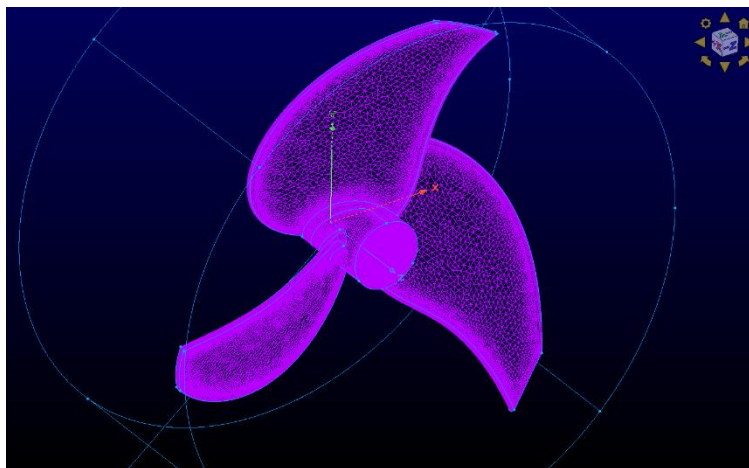
Figure 3.15 (c) shows the surface mesh of the propeller which is clustered at the leading and the trailing edges where flow separation is expected.



(a)

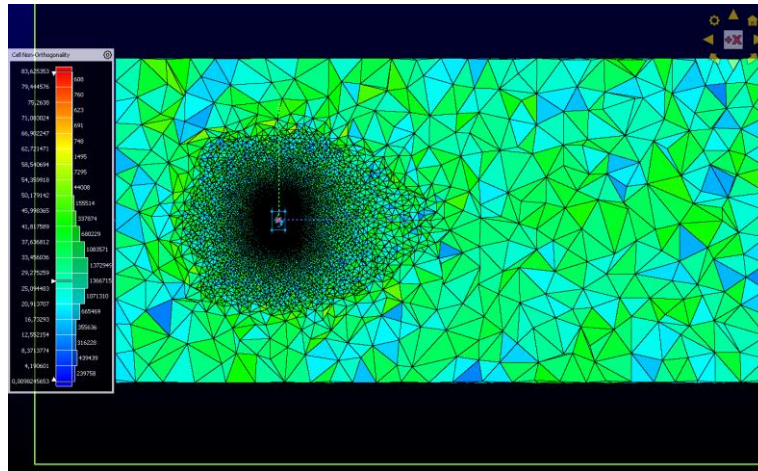


(b)

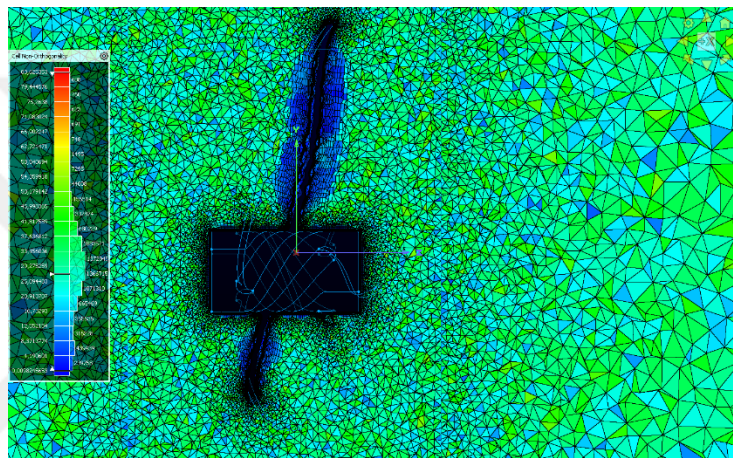


(c)

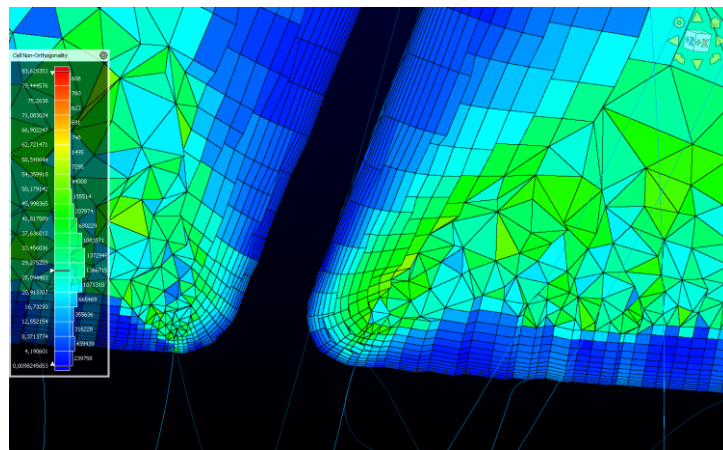
Figure 3.15: 3D Flow field boundary and stator and rotor regions (a) Flow field boundaries and surface mesh. (b) Rotational region. (c) Propeller surface mesh.



(a)



(b)



(c)

Figure 3.16: General representation of flow domain and details of computational mesh. (a) General domain section @ $x = 0$. (b) Mesh detail inside the rotational region. (c) prism cells around Blade hub inside the boundary layer.

Figure 3.16 shows the cross section of the flow domain in which computational mesh is denser around the rotating part of the domain. Especially in Figure 3.16 (c) one can see the high resolution structured computational cells scaled according to the appropriate y^+ value demanded by the turbulence model.

The Reynolds number (Re) is a dimensionless quantity that is used to characterize the flow of a fluid. It is defined as the ratio of inertial forces to viscous forces and is given by:

$$Re = (\rho * v * L) / \mu \quad (13)$$

where:

- ρ is the density of the fluid
- v is the velocity of the fluid
- L is a characteristic length scale of the flow (e.g., diameter of a pipe)
- μ is the dynamic viscosity of the fluid

To calculate $y^+=1$ based on Reynolds number, you need to first calculate the shear velocity (u^*):

$$u^* = (\tau_w / \rho)^{0.5} \quad (14)$$

where τ_w is the wall shear stress. The wall shear stress is calculated during the simulations.

Once u^* and τ_w , are calculated then one can calculate the dimensionless distance from the wall, y^+ , using the following formula:

$$y^+ = y * u^* / \nu \quad (15)$$

where y is the distance from the wall, and ν is the kinematic viscosity of the fluid.

3.4.1. Meshing

Preparing a meshing strategy is an important step in the design and optimization of propellers for submersible mixers. There are some details to consider when preparing a meshing strategy.

The first step is to identify the important features of the propeller and the surrounding fluid domain. This could include the propeller blades, the hub, the inflow and outflow boundaries and any other geometric features that may impact the flow. Once the important features have been identified, choose a suitable meshing technique that can accurately capture the flow physics. This could include structured or unstructured meshes, depending on the complexity of

the geometry and the desired level of resolution. The next step is to determine the appropriate mesh resolution for the different regions of the domain. This could involve using a mesh sensitivity analysis to ensure that the mesh is fine enough to capture important flow features but not so fine that it leads to excessively long simulation times. When preparing the mesh, it's important to consider the boundary conditions for the simulation. For example, if the propeller is immersed in a tank of liquid, the boundary condition at the interface between the propeller and the fluid will need to be carefully defined. After generating the mesh, it's important to verify the mesh quality to ensure that it meets certain criteria, such as mesh skewness, aspect ratio, and orthogonality. Poor mesh quality can lead to inaccurate or unstable simulations. If necessary, refine the mesh in regions where the flow physics are particularly complex or where the mesh quality is poor. This can be done using local mesh refinement techniques or by manually adjusting the mesh.

By following these steps, a meshing strategy can be developed that accurately captures the flow physics around the propeller and allows for accurate simulations of its performance. This can help optimize the design of the propeller for maximum mixing efficiency and energy consumption.

3.4.2. Simulation Model & Boundary Conditions

Averaging the momentum equation over a statistically stationary time interval, the Reynolds stresses defining the turbulence in the flow field can be modelled. After the averaging operation is applied to both sets of equations which are momentum and continuity equations. A new set of equations emerges which is known as Reynolds Averaged Navier-Stokes (RANS) equations. The incompressible RANS equation sets are as follows:

Continuity Equation:

$$(\nabla \cdot (\rho \bar{\mathbf{u}})) = 0 \quad (16)$$

Momentum Equation:

$$\frac{\partial(\rho \bar{\mathbf{u}})}{\partial t} + \nabla \cdot (\rho \bar{\mathbf{u}} \otimes \bar{\mathbf{u}}) = -\nabla \bar{p} + \nabla \cdot \bar{\boldsymbol{\tau}} + \rho \mathbf{g} + \nabla \cdot (\overline{\boldsymbol{\sigma}_t}) \quad (17)$$

The Reynolds Stress expressed above is the term $\nabla \cdot (\overline{\boldsymbol{\sigma}_t})$ on the right-hand side of the equation. In this case, to solve the flow, ten unknowns must be solved with these four equations

(one continuity and three momentum equations). However, since it is impossible to solve ten unknowns with four equations, this problem is known as the closure problem. Therefore, Reynolds Stress terms need to be modeled to solve the flow. Models are used to solve this problem, which has not been solved until now, with unknown sizes with known ones.

The non-linear terms created by the turbulence stresses were modelled using the k-Omega SST model. (Menter, F., 1993). In this study, the pimpleFoam and simpleFoam solvers of OpenFOAM are used. Boundary conditions and computational domain are given in Figure 3.17

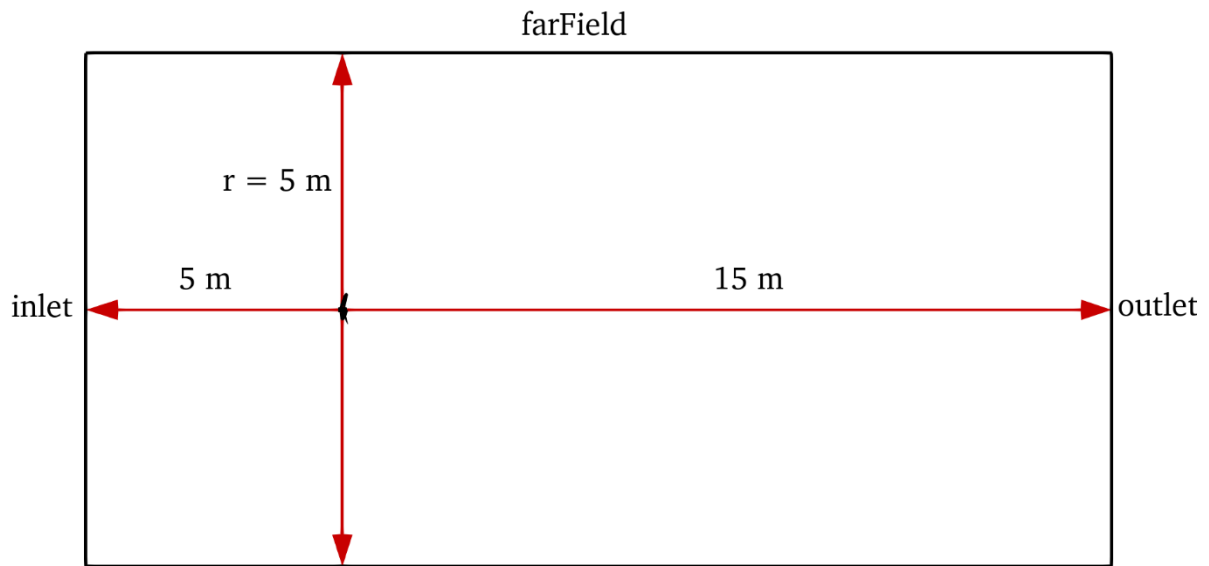


Figure 3.17: Calculation Area and Boundary Conditions

The boundary conditions are given as “totalPressure” for pressure at the inlet and “fixedValue” for the outlet. The boundary conditions for Velocity are defined as “pressure Inlet Outlet Velocity” at the inlet, and as “inlet Outlet” at the outlet. The Boundary Conditions for pressure, velocity, turbulent kinetic energy and omega are given in Table 1.

Table 1: The Boundary Conditions for Pressure, Velocity, Turbulent Kinetic Energy and Omega

Boundries	U	p	k	omega
inlet	pressureInletOutletVelocity	totalPressure	fixedValue	fixedValue
outlet	inletOutlet	fixedValue	inletOutlet	inletOutlet
farField	noSlip	zeroGradient	kqRWallFunction	omegaWallFunction
propeller	noSlip	zeroGradient	kqRWallFunction	omegaWallFunction
AMI rotor/stator	cyclicAMI	cyclicAMI	cyclicAMI	cyclicAMI

OpenFOAM files used for boundary conditions are shared in appendix.

The solution domain and boundary conditions are important components of any computational fluid dynamics (CFD) simulation of the flow around a propeller of a submersible mixer in a biogas plant. The solution domain refers to the physical region over which the simulation is performed, while the boundary conditions describe the behavior of the fluid at the edges of the domain. Here are some details on each:

Solution Domain: The solution domain for the simulation will typically include the propeller, the fluid domain surrounding the propeller, and any other relevant components of the system such as a tank or other structures. The solution domain will typically be discretized using a mesh, with the resolution of the mesh varying depending on the level of detail required for the simulation.

Boundary Conditions: Boundary conditions define the behavior of the fluid at the edges of the solution domain. In the case of a submersible mixer in a biogas plant, the boundary conditions will depend on the specific geometry of the system and the type of simulation being performed. Some typical boundary conditions might include:

Inflow boundary condition: This describes the behavior of the fluid as it enters the domain, and may be specified as a constant velocity or mass flow rate. In some cases, a velocity profile may be prescribed based on experimental data or previous simulations.

Outflow boundary condition: This describes the behavior of the fluid as it leaves the domain, and may be specified as a zero-gradient boundary condition, a constant pressure boundary condition, or a velocity profile.

Wall boundary condition: This describes the behavior of the fluid in contact with a solid surface, such as the propeller or the walls of a tank. This boundary condition may be specified as a no-slip boundary condition, which assumes that the velocity of the fluid at the wall is zero, or as a slip boundary condition, which allows for some degree of slip between the fluid and the wall.

Symmetry boundary condition: This describes the behavior of the fluid at a plane of symmetry in the domain, and may be used to reduce the size of the computational domain or to simplify the simulation.

By carefully selecting the solution domain and boundary conditions, and by applying appropriate numerical methods to solve the Navier-Stokes equations, CFD simulations can provide valuable insight into the flow behavior around a submersible mixer propeller, and can

be used to optimize the design of the propeller for maximum mixing efficiency and energy efficiency.

3.5. Running Simulations

After the steps described in section 3.4.1 and 3.4.2, the simulation is ready to run. However, the design set scanning and optimization studies need to be put in a loop. This cycle is given in Figure 3.18. The aim here is to understand the sensitivity of design outputs to design inputs.

In the study, 3 different outputs showing mixer performance were examined.:

- Thrust
- Power
- Thrust per unit power

The stages of the process in which the outputs given above are obtained are as follows: creating the blade geometry drawn according to the predetermined parameters, creating different designs of these blade geometries according to the design parameters, creating a solution network for each design and making simulations with CFD software, calculating the design outputs from the simulation results, and converting the outputs to the inputs. It can be summarized as optimizing the design by looking at its sensitivity and passing it through network and CFD analyzes again.

The CAESES software used for geometry creation in Section 0 also communicates with OpenFOAM for CFD analysis and with Pointwise for the creation of the necessary mesh, and forms the framework of the loop given in Figure 3.18. CAESES can commands external software, it communicates with and can read the outputs from these software. Scripts that need to be run for this work flow have been prepared.

In order to achieve the targeted outputs, 7 different design parameters were used in the creation of the designs. The maximum and minimum points of these design parameters are determined and the number of different points to be taken between these two values is entered into the software. In the scope of this project, the number of parameters was kept high and the value range of these parameters was kept low, since it was desired to see how sensitive they are to how many different parameters. The design parameters and extreme points are given in the

table below (Within the scope of this project, different designs were obtained by keeping the primary effective parameter constant and making changes on the secondary effective parameters).

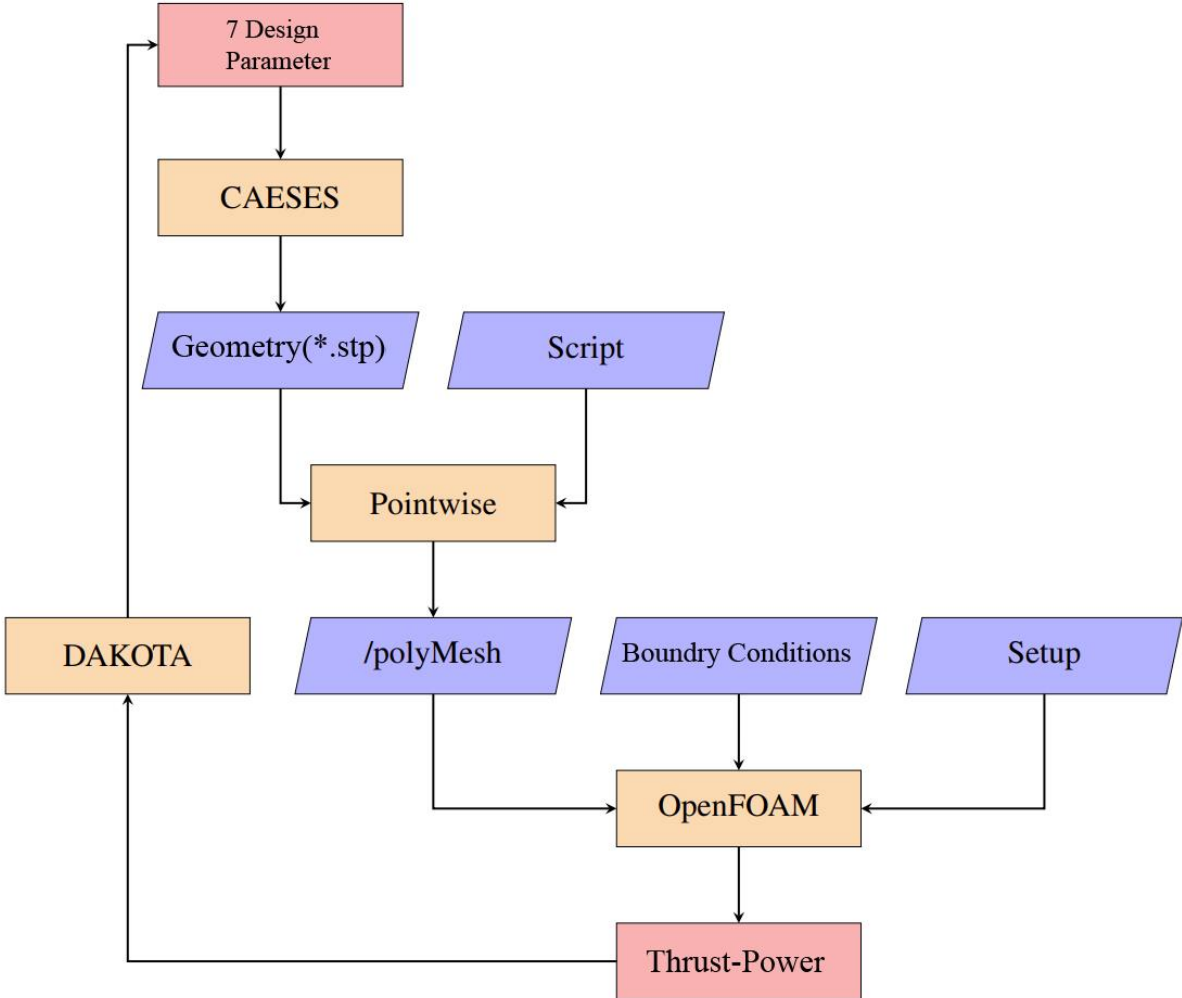


Figure 3.18: Optimization flowchart

128 different designs were created for each model with the parameters entered in CAESES. For each created design, a process starts with the application file named “run.bat” respectively. The run.bat file connects to the server of the local machine where CAESES is used and runs the “Allrun” (Annex C) file that will run the next processes on the server. The mesh macro as input to CAESES and all scripts OpenFOAM requested for analysis were defined according to the file directory OpenFOAM requested. The process after the geometry is created and exported is performed on the server by the Allrun script.

4. RESULTS

In this section, the results of CFD analysis of the investigated designs, whose pre-processing steps are given in section 3.4, will be examined.

The results obtained with the analyzes are given in three stages. First of all, the general flow pattern of a mixer is given with the qualitative data obtained through a sample design, and then the quantitative results are investigated at a more detailed level (i.e. design performance metrics were examined). In **Table 2** boundaries of the parameter space is given.

Table 2: Design parameters, limit points and number of selected points

Design parameters	Min.	Max.	Quantity
Propeller Diameter [m]	0,68	0,72	2
Pitch [°]	30	34	2
Camber	0,02	0,02	2
Camber Position	0,45	0,55	2
Blade Area [m ²]	0,64	0,68	2
Tip Chord Length	0,2	0,4	2
Radial position of largest chord	0,48	0,54	2

The effect of the mixer on the downstream and the mixing performance were investigated using the three velocity components u_r , u_t , u_a (radial, tangential and axial) in cylindrical coordinates. These quantities are averaged spatially and temporarily over the tangential direction and time. In addition, by examining the pressure coefficient in 4 different blade sections, low pressure regions formed on the suction and pressure surfaces were observed.

Thrust force, power value and ratio of thrust force to power of the mixer propeller are given in the optimization tables.

4.1. Sample Simulation Results

In this section, sample outputs prepared by processing the raw data, obtained while traversing the design space, were given.

The qualitative flow field of an exemplary design is shown in Figure 4.1. Here, it is seen that the flow area is generally settled and it collects the fluid from an area larger than the propeller diameter on the flow and directs it to the downstream, within expectations. The quantitative results of the flow field are also given in Figure 4.3 below.

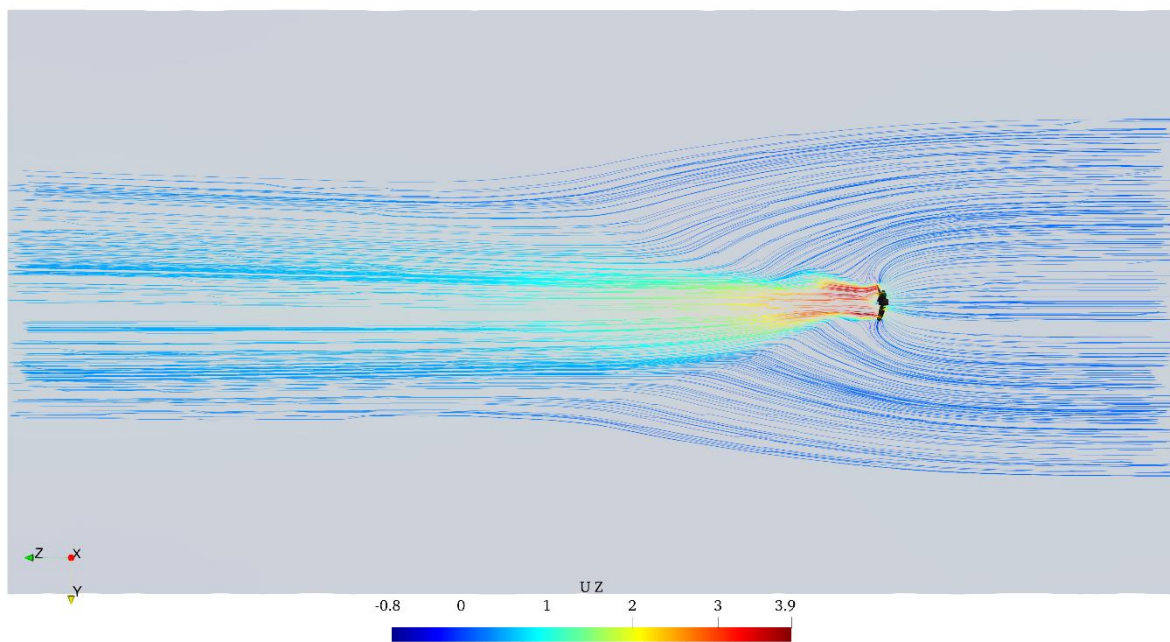


Figure 4.1: Streamlines

In general, the reason why such a flow field is seen in axial type rotary machines is the pressure difference obtained between the suction and discharge surfaces over the blades. This pressure difference is also given in Figure 4.2 qualitatively over an exemplary design. The quantitative analysis of this effect is given in Figure 4.5 on the C_p graph.

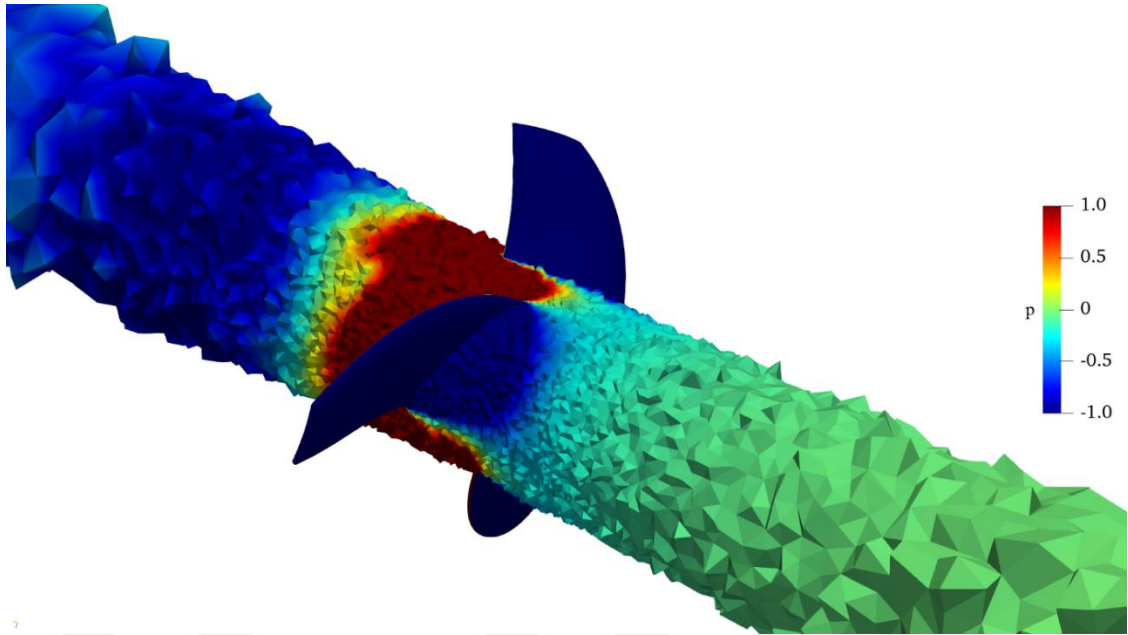
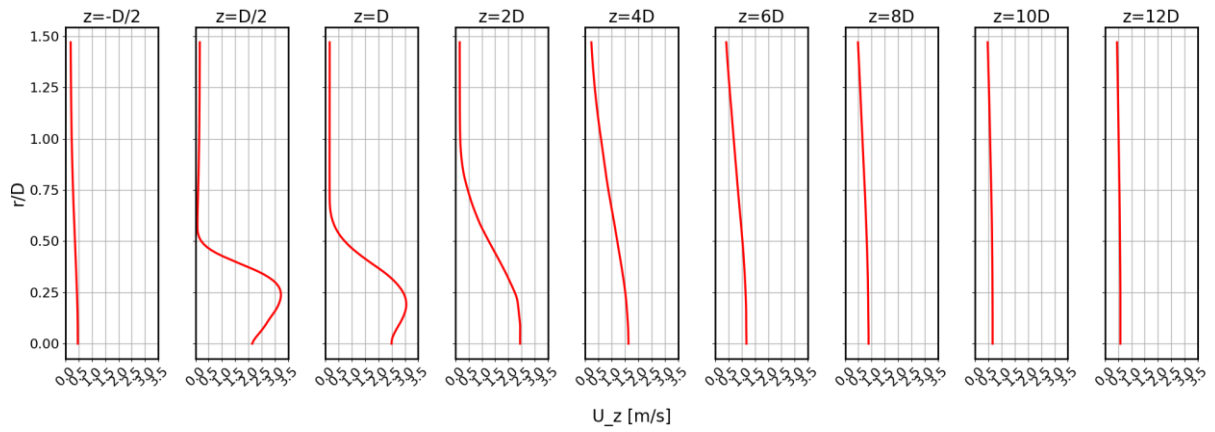
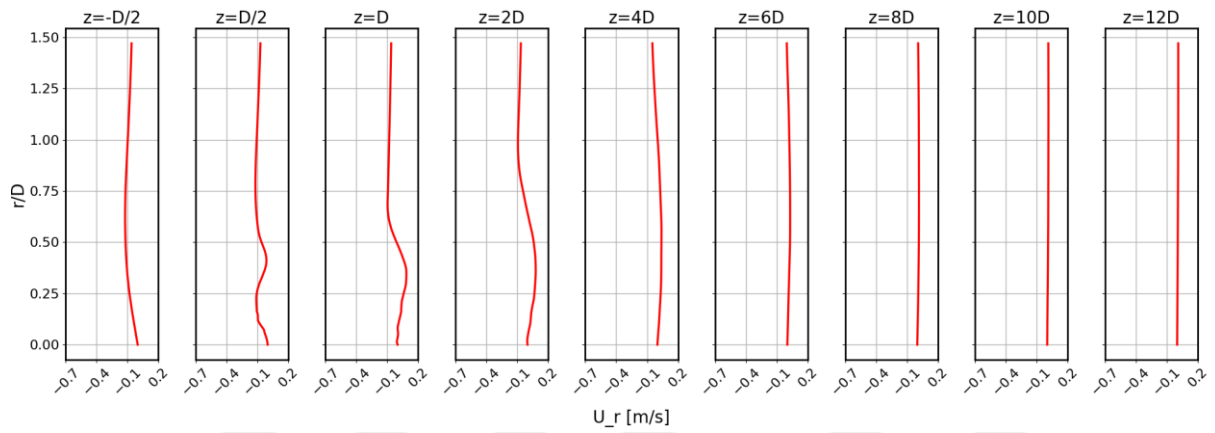


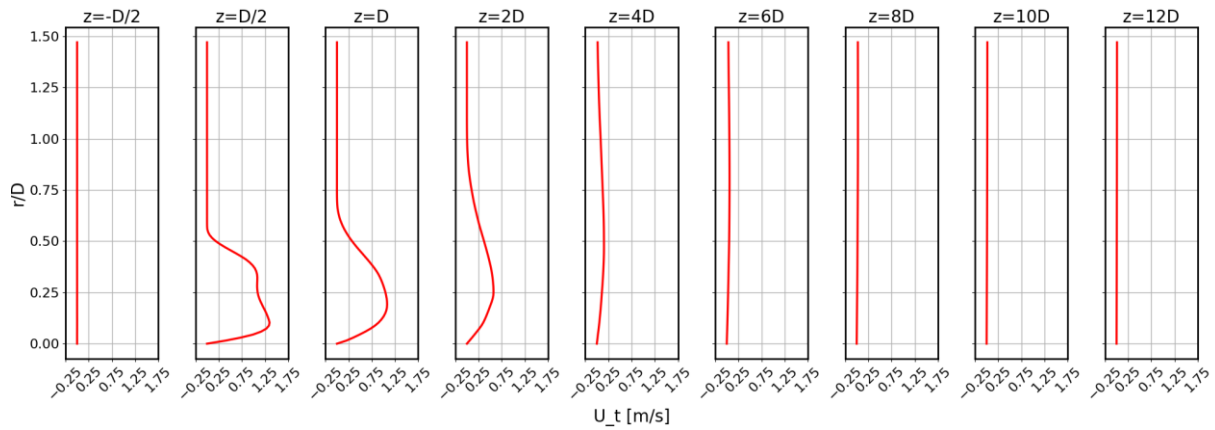
Figure 4.2: Pressure distribution in cylindrical section



(a)



(b)

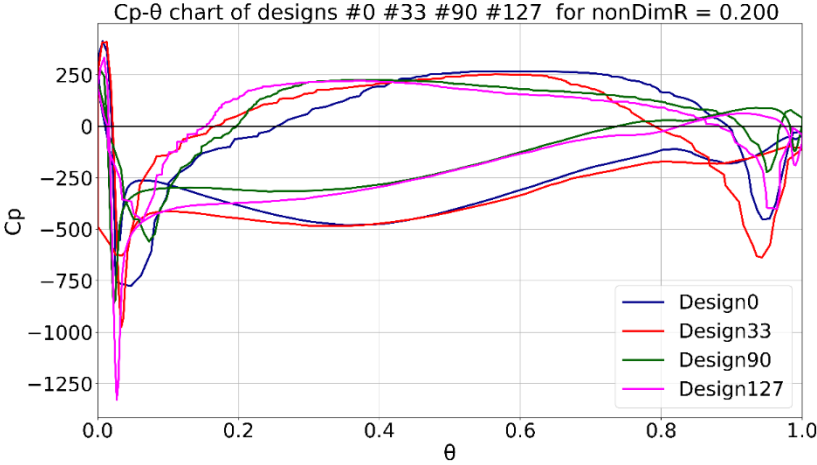


(c)

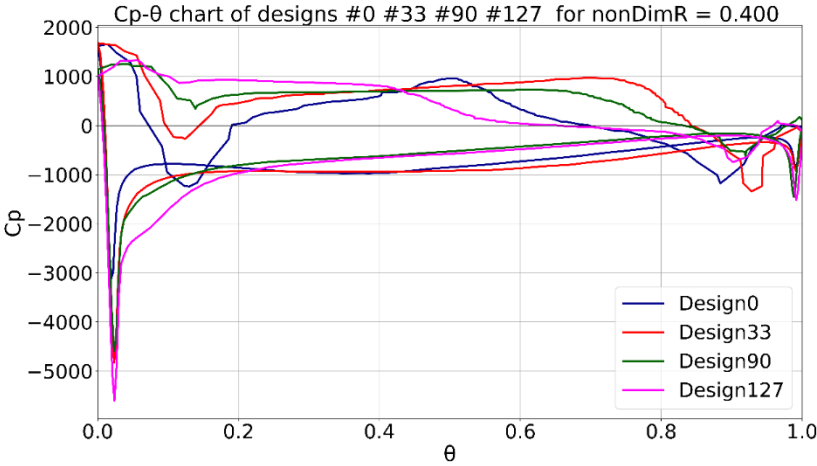
Figure 4.3: Speed profiles under flow. (a) Axial Speeds. (b) Radial Speeds. (c) Tangential speeds

Figure 4.3 shows the tangentially averaged velocities in the downstream region of the impeller. For tangential, radial and axial velocity, a graph was drawn by taking the velocity at its apse and the value of 7 points in the local radii of these cross-sections in its ordinate, separately for all sections at 9 different distances from the diameter.

As it can be seen in Figure 4.3 (a), the highest axial velocity was reached at $r/D = 0.25$ at $D/2$ distance. It is seen in Figure 4.3 (b), that this velocity also spreads in the radial direction as it moves in the downstream direction.



(a)



(b)

Figure 4.4: Pressure coefficient distributions in 4 radial sections of 4 different designs. (a) $r/R = 0.2$ (b) $r/R = 0.4$

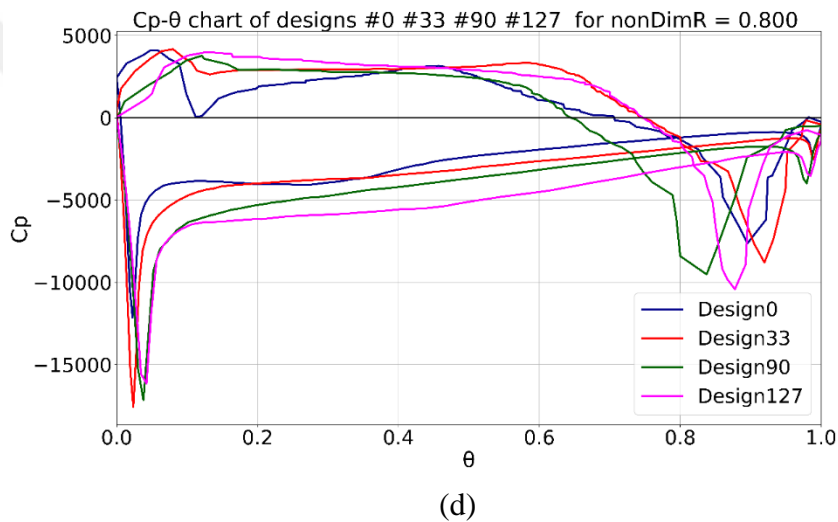
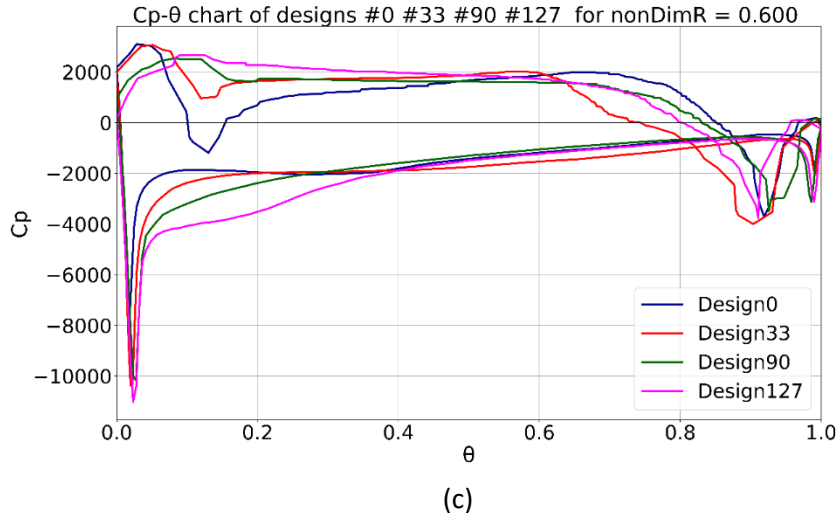


Figure 4.5: Pressure coefficient distributions in 4 radial sections of 4 different designs. (c) $r/R = 0.6$, (d) $r/R = 0.8$

Another graph to look at to examine propeller performance is the C_p vs x/c graph seen in Figure 4.5. While the abscissa shows the nondimensionalized distance with the blade axis, the ordinate axis has the C_p value, which shows the pressure difference at that point with respect to the atmospheric pressure.

4.2. Sensitivity Results

A design set for each model is created by looping the simulation template in Figure 3.18 and using different input parameters, the method of which is described in section 3.4 and the results are given in section 4.1.

In Figure 4.6, Figure 4.7 and Figure 4.8, the limits of these design sets and the thrust, power and efficiency values obtained as a result of simulations are given. In general, it is seen that the 300 N/kW efficiency value determined within the scope of this project for fast mixers has been achieved in the simulations.

These results constitute the first stage of the optimization work and establish the state space that will be used for possible future studies. Based on the state space created in the second stage, the efficiency value obtained by various optimization algorithms will be improved.

Design Set	hatve	kanatAlani	ucGenisligi	kokGenisligi	thrust2Power	T_N	P_kW	PowerLimit
Dakota_03_des0060	n/a	n/a	n/a	n/a	n/a	n/a	n/a	n/a
Dakota_03_des0014	35	0.60885106	0.2794329	0.32802747	-350.73698	-1690.4296	4.8196504	4.8196504
Dakota_03_des0002	35	0.65248087	0.26382292	0.36538692	-349.75723	-1719.9392	4.917523	4.917523
Dakota_03_des0030	35	0.66524545	0.27398213	0.41294598	-349.66144	-1733.9459	4.9589281	4.9589281
Dakota_03_des0021	36	0.59507234	0.26898132	0.35252741	-338.85331	-1710.7277	5.0485791	5.0485791
Dakota_03_des0047	36	0.63077794	0.30444867	0.3388341	-339.38889	-1747.768	5.1497502	5.1497502
Dakota_03_des0011	36	0.63186018	0.2989131	0.37881869	-339.03569	-1755.2333	5.1771343	5.1771343
Dakota_03_des0027	36	0.63514377	0.30800361	0.48252481	-339.39849	-1763.0373	5.1945938	5.1945938
Dakota_03_des0042	36	0.61476141	0.3579178	0.39690799	-339.01983	-1761.4942	5.1958442	5.1958442
Dakota_03_des0057	36	0.62952898	0.35503119	0.33321851	-338.53716	-1779.2173	5.2556041	5.2556041
Dakota_03_des0007	36	0.66360708	0.32456734	0.40494582	-338.86402	-1789.8496	5.2819111	5.2819111
Dakota_03_des0010	36	0.66872577	0.30990654	0.36573325	-339.89836	-1800.7601	5.297937	5.297937
Dakota_03_des0034	37	0.59532998	0.30679055	0.44727386	-328.77418	-1761.143	5.356695	5.356695
Dakota_03_des0053	37	0.61192908	0.2673335	0.47822356	-329.17839	-1788.1527	5.4321691	5.4321691
Dakota_03_des0039	37	0.60670845	0.3997295	0.34207107	-329.67658	-1801.9783	5.4658972	5.4658972
Dakota_03_des0040	37	0.5917797	0.39467131	0.42346889	-328.12622	-1794.1407	5.4678371	5.4678371
Dakota_03_des0043	37	0.673288	0.34246012	0.47115737	-328.33226	-1883.3027	5.7359661	5.7359661
Dakota_03_des0050	38	0.6186203	0.2271121	0.38136529	-317.91063	-1829.1803	5.7537564	5.7537564
Dakota_03_des0004	38	0.63798143	0.20727541	0.31440183	-317.91229	-1849.5242	5.8177185	5.8177185
Dakota_03_des0026	39	0.60725654	0.26104464	0.30862501	-307.32422	-1859.6371	6.0510594	6.0510594
Dakota_03_des0024	39	0.66998558	0.21200624	0.31691981	-306.50882	-1949.4156	6.3600636	6.3600636
Dakota_03_des0017	39	0.65619023	0.30006814	0.39525805	-306.38867	-1956.8239	6.3867371	6.3867371
Dakota_03_des0020	39	0.67672906	0.24033923	0.3843999	-306.57476	-1967.804	6.4186759	6.4186759
Dakota_03_des0019	40	0.59289202	0.3610453	0.42840135	-297.60273	-1920.2922	6.4525357	6.4525357
Dakota_03_des0015	40	0.62199926	0.24158534	0.38306713	-296.849	-1924.4183	6.4828188	6.4828188
Dakota_03_des0005	40	0.62874017	0.34382184	0.34948257	-296.77572	-1971.0769	6.6416381	6.6416381
Dakota_03_des0041	40	0.63079051	0.32539537	0.41566803	-296.42529	-1969.967	6.6457453	6.6457453
Dakota_03_des0052	40	0.65313872	0.28725355	0.30259791	-296.23472	-1984.7123	6.6997964	6.6997964
Dakota_03_des0049	41	0.59580234	0.24771944	0.44822355	-287.51518	-1929.9292	6.7124428	6.7124428
Dakota_03_des0001	41	0.61812852	0.2410391	0.32172459	-287.28263	-1942.2201	6.7606598	6.7606598
Dakota_03_des0016	40	0.65046159	0.39333023	0.4540227	-296.63847	-2021.7334	6.8154794	6.8154794
Dakota_03_des0059	41	0.59256926	0.34704355	0.32393369	-287.33011	-1959.3604	6.8191962	6.8191962
Dakota_03_des0037	41	0.62813309	0.28384049	0.36799698	-287.0402	-1987.0256	6.9224645	6.9224645
Dakota_03_des0003	41	0.66955513	0.28294446	0.32640378	-286.78449	-2046.0592	7.1344834	7.1344834
Dakota_03_des0035	41	0.67797015	0.25295194	0.31600713	-286.89007	-2053.5094	7.1578267	7.1578267
Dakota_03_des0031	41	0.65980679	0.36422943	0.43867244	-286.71207	-2065.605	7.2044577	7.2044577
Dakota_03_des0056	42	0.63694953	0.20093537	0.41126663	-278.57364	-2011.7595	7.2216435	7.2216435
Dakota_03_des0032	42	0.60916865	0.35676684	0.30527987	-277.88975	-2018.0205	7.2619466	7.2619466
Dakota_03_des0045	42	0.62302689	0.31633238	0.36692991	-277.71202	-2031.0702	7.313584	7.313584
Dakota_03_des0029	43	0.60220876	0.28227816	0.36403538	-269.67408	-1972.9386	7.3160113	7.3160113
Dakota_03_des0008	43	0.59871607	0.21019471	0.47314854	-270.60689	-1987.6005	7.3449739	7.3449739
Dakota_03_des0046	43	0.58372348	0.32682767	0.36007266	-269.137	-1983.5302	7.3699647	7.3699647

Figure 4.6: DK75 Design set results

	pervaneCapi	hatve	enGenisRadyalPozisyon	kanatAlani	ucGenisligi	kamburluk	kamburlukShift	T_N	thrust2Power	P_kw
Ehx...0002	0.68	30	0.48	0.64	0.2	0.05	0	-2419.9254	-381.58519	6.3417696
Ehx...0010	0.68	30	0.48	0.68	0.2	0.05	0	-2476.4192	-379.54243	6.5247494
Ehx...0003	0.68	30	0.48	0.64	0.2	0.05	0.1	-2447.5748	-373.68743	6.5497916
Ehx...0018	0.68	30	0.54	0.64	0.2	0.05	0	-2693.9574	-372.02263	7.2413805
Ehx...0011	0.68	30	0.48	0.68	0.2	0.05	0.1	-2512.3458	-371.48761	6.7629329
Ehx...0026	0.68	30	0.54	0.68	0.2	0.05	0	-2747.79	-369.21032	7.4423434
Ehx...0000	0.68	30	0.48	0.64	0.2	0.02	0	-2073.7157	-367.75358	5.6388729
Ehx...0008	0.68	30	0.48	0.68	0.2	0.02	0	-2135.186	-367.00023	5.8179418
Ehx...0006	0.68	30	0.48	0.64	0.2	0.05	0	-2524.6727	-365.90143	6.8998711
Ehx...0016	0.68	30	0.54	0.64	0.2	0.02	0	-2369.9335	-365.6512	6.481405
Ehx...0019	0.68	30	0.54	0.64	0.2	0.05	0.1	-2738.9606	-365.47366	7.4942762
Ehx...0014	0.68	30	0.48	0.68	0.2	0.05	0	-2576.3783	-364.73978	7.0636056
Ehx...0024	0.68	30	0.54	0.68	0.2	0.02	0	-2434.0875	-364.47079	6.6784159
Ehx...0004	0.68	30	0.48	0.64	0.2	0.02	0	-2181.9855	-363.31145	6.0058265
Ehx...0027	0.68	30	0.54	0.68	0.2	0.05	0.1	-2794.1032	-362.18412	7.7145933
Ehx...0020	0.68	30	0.54	0.64	0.2	0.02	0	-2347.1947	-362.16928	6.4809326
Ehx...0022	0.68	30	0.54	0.64	0.2	0.05	0	-2707.5386	-362.11699	7.476972
Ehx...0066	0.72	30	0.48	0.64	0.2	0.05	0	-3008.5822	-362.0808	8.3091458
Ehx...0012	0.68	30	0.48	0.68	0.2	0.02	0	-2231.9377	-361.89993	6.1672781
Ehx...0028	0.68	30	0.54	0.68	0.2	0.02	0	-2378.8894	-361.47044	6.5811451
Ehx...0001	0.68	30	0.48	0.64	0.2	0.02	0.1	-2096.0635	-361.42037	5.7995168
Ehx...0030	0.68	30	0.54	0.68	0.2	0.05	0	-2784.1789	-361.20957	7.7079322
Ehx...0007	0.68	30	0.48	0.64	0.2	0.05	0.1	-2561.7763	-360.74081	7.101432
Ehx...0009	0.68	30	0.48	0.68	0.2	0.02	0.1	-2154.6462	-360.08241	5.9837585
Ehx...0074	0.72	30	0.48	0.68	0.2	0.05	0	-3083.6665	-360.05034	8.5645428
Ehx...0015	0.68	30	0.48	0.68	0.2	0.05	0.1	-2624.7151	-359.21726	7.3067622
Ehx...0005	0.68	30	0.48	0.64	0.2	0.02	0.1	-2198.4266	-358.78461	6.1274272
Ehx...0017	0.68	30	0.54	0.64	0.2	0.02	0.1	-2390.0368	-358.62818	6.6643864
Ehx...0025	0.68	30	0.54	0.68	0.2	0.02	0.1	-2459.9185	-357.05643	6.889439
Ehx...0021	0.68	30	0.54	0.64	0.2	0.02	0.1	-2375.4165	-357.00917	6.6536569
Ehx...0013	0.68	30	0.48	0.68	0.2	0.02	0.1	-2245.139	-356.9503	6.2897803
Ehx...0023	0.68	30	0.54	0.64	0.2	0.05	0.1	-2764.0892	-356.67826	7.7495309

Figure 4.7: DK110 Design set results.

	pervaneCapi	hatve	enGenisRadyalPozisyon	kanatAlani	ucGenisligi	kamburluk	kamburlukShift	T_N	thrust2Power	P_kw
Ens...0003	0.76	30	0.48	0.7	0.15	0.04	0	-3616.6544	-349.6789	10.342787
Ens...0004	0.76	30	0.48	0.7	0.15	0.04	0.1	-3658.4689	-344.40825	10.622478
Ens...0021	0.76	30	0.52	0.7	0.15	0.04	0	-3928.0828	-343.90065	11.422144
Ens...0012	0.76	30	0.48	0.7	0.3	0.04	0	-3758.0597	-342.32058	10.978188
Ens...0000	0.76	30	0.48	0.7	0.15	0.02	0	-3285.1784	-340.31687	9.6529298
Ens...0022	0.76	30	0.52	0.7	0.15	0.04	0.1	-3994.566	-339.1271	11.778964
Ens...0005	0.76	30	0.48	0.7	0.15	0.04	0.2	-3746.5794	-338.26249	11.075953
Ens...0030	0.76	30	0.52	0.7	0.3	0.04	0	-3993.6401	-338.00631	11.815283
Ens...0013	0.76	30	0.48	0.7	0.3	0.04	0.1	-3800.0577	-337.8114	11.249051
Ens...0075	0.8	30	0.48	0.7	0.15	0.04	0	-4903.624	-336.5217	13.382863
Ens...0018	0.76	30	0.52	0.7	0.15	0.02	0	-3654.8368	-336.23588	10.86986
Ens...0009	0.76	30	0.48	0.7	0.3	0.02	0	-3401.7573	-335.19516	10.148587
Ens...0027	0.76	30	0.52	0.7	0.3	0.02	0	-3650.4874	-334.62096	10.909321
Ens...0031	0.76	30	0.52	0.7	0.3	0.04	0.1	-4048.9084	-334.18961	12.115602
Ens...0023	0.76	30	0.52	0.7	0.15	0.04	0.2	-4091.0871	-332.37443	12.30867
Ens...0076	0.8	30	0.48	0.7	0.15	0.04	0.1	-4576.3433	-331.54445	13.803106
Ens...0014	0.76	30	0.48	0.7	0.3	0.04	0.2	-3870.3805	-331.40347	11.678757
Ens...0093	0.8	30	0.52	0.7	0.15	0.04	0	-4922.389	-330.87537	14.876868
Ens...0001	0.76	30	0.48	0.7	0.15	0.02	0.1	-3320.0296	-330.32219	10.050883
Ens...0084	0.8	30	0.48	0.7	0.3	0.04	0	-4675.8911	-329.19025	14.204221
Ens...0007	0.76	30	0.48	0.7	0.15	0.06	0.1	-4033.4316	-329.01997	12.258926
Ens...0032	0.76	30	0.52	0.7	0.3	0.04	0.2	-4145.9858	-328.34696	12.626844
Ens...0094	0.8	30	0.52	0.7	0.15	0.04	0.1	-4980.4462	-325.98693	15.278055
Ens...0028	0.76	30	0.52	0.7	0.3	0.02	0.1	-3713.6749	-325.9017	11.395077
Ens...0102	0.8	30	0.52	0.7	0.3	0.04	0	-4982.0016	-325.83879	15.289775
Ens...0010	0.76	30	0.48	0.7	0.3	0.02	0.1	-3430.814	-325.72234	10.53294
Ens...0072	0.8	30	0.48	0.7	0.15	0.02	0	-4098.5724	-325.51593	12.591004
Ens...0024	0.76	30	0.52	0.7	0.15	0.06	0	-4268.0875	-324.61121	13.148306
Ens...0077	0.8	30	0.48	0.7	0.15	0.04	0.2	-4659.9097	-324.44325	14.362788
Ens...0085	0.8	30	0.48	0.7	0.3	0.04	0.1	-4726.2798	-324.25862	14.575649

Figure 4.8: DK150 Design set results.

In the design researches, it was desired to make two different design comparisons for 2 different power groups. In the designs given in the table, thrust/power values that can present thrust moment and efficiency expressions are seen.

Table 3: Design Results Thrust, Moment, Power, Thrust/Power

Design Name	Thrust [N]	Moment [Nm]	Power [kW]	Thrust/Power [N/kW]
DK11_des000	3015.03	261.77589	8.909259807	338.42
DK11_des001	3351.50	300.89	10.24	327.28
DK15_des000	4048.91	383.8913	13.06	310.02
DK15_des001	4586.78	435.75	14.83	309.29

There is no change in the primary parameters between DK11_des000 and DK11_des001, but the effect of the change in the position of the largest cord of the blade in the radial direction is seen.

There is no change in the primary parameters between DK15_des000 and DK15_Des001, but the effect of the change in the humps of the blade section profiles is seen.



5. DISCUSSION

It can be seen in Figure 4.3 (a) that the axial velocities in the downstream direction continue at $r/D=0.75$ up to a distance of $8D$. It can be said that this mixer has not only a directing speed but also an accelerating effect even at $8D$ distance. As a matter of fact, it lost its accelerator effect at $10D$ and $12D$ distances and continued only at a directing speed. Since the axial velocity is the velocity that determines the thrust force of the flow, the physical explanation for accelerating the velocities up to $8D$ distance in this way is an indication that the flow propelled by the thrust force is accelerated up to that distance.

In Figure 4.5, C_p indicates the suction side on the propeller in negative values and the pressure side in positive values. The slope of the graph shows the pressure change rate and the characteristic of the flow. A straight line indicates that the pressure distribution is smooth and the flow is symmetrical, while an increase in the slope of the curve indicates that there are pressure differences and the flow is asymmetrical. Since the sudden increase of the curve slope indicates a sudden change in the pressure gradient, it should be checked whether there is a flow separation at that point.

In Figure 4.5, the pressure coefficients of 4 different designs on the impeller at different r sections are given. Pressure coefficient curves of Design0, Design33, Design90 and Design127 are given. As stated before, sudden pressure changes in the C_p curve along the chord are undesirable. Another parameter gives the lift coefficient value of the area under the suction side and pressure side curves in the C_p graph. The area between the two curves should be maximum, but this means a sudden increase in the pressure gradient, causing flow separations and performance losses. In this case, the most optimum situation for the design should be provided among the options. In Figure 4.5 (a), while the area Design0 is the largest, flow separation may have occurred due to the sudden pressure change close to $\theta=0.9$. In Figure 4.5 (b), the areas of almost all designs are equal. The design with the largest area in Figure 4.5 (c) and Figure 4.5 (d) is Design127.

Figure 4.5, four different designs are given: Design0, Design33, Design90 and Design127. These four different designs were selected from the design set as a result of the optimization studies carried out in CAESES, based on thrust, power, torque and thrust produced per power.

The blade geometry variables specified in Figure 3.1 is given as input parameters, and the sensitivity analysis was performed with the output parameters Thrust, Moment, Power and Thrust per unit power. Input parameters were changed at regular intervals and their effects on the outputs were examined in Table 3 and sensitivity analysis of geometries created with different input parameters in CAESES is shown in Figure 4.6, Figure 4.7, Figure 4.8 . As a result of the sensitivity analysis, the most sensitive parameter was pitch. When the pitch value increases too much, the thrust to power ratio decreases, and when the pitch value decreases, it also decreases. Because of this, attention was paid to the pitch parameter and accordingly the pitch value that produced the highest thrust to power ratio was selected.

Figure 5.1 shows the results of a sensitivity analysis performed in the CAESES software. An analysis has been made showing the effects of propeller diameter, pitch, tip chord length, tip width, camber and camber shift values of the propeller as input on thrust to power, thrust and power parameters selected as output. As the propeller diameter increased, thrust increased, thrust to power decreased, and power decreased. As the pitch increases; Thrust to power decreased while thrust and power increased. There is also a pitch-like result when the tip chord length increases. Since the tip width was changed in a very small range, very little change was observed on the outputs. The hump also exhibited a change like pitch. Here it is concerned with the quantitative quantities of state changes to be compared, since they all provide the same characteristic state as change. The background color of each graph is indicative of the amount of change corresponding to those parameters. Accordingly, since the greenest color for Thrust shows the steepest variation, this corresponds to the propeller diameter. For thrust to power, the most change occurs in pitch, while the propeller diameter is the most sensitive for power. As a result, pitch is the most sensitive parameter to thrust to power as a result of this sensitivity analysis. When the pitch increases too much, the thrust to power increases a lot, and when it decreases, it decreases. Therefore, if the thrust to power variable is chosen as the main variable in the design, the most important parameter to be considered is the pitch.

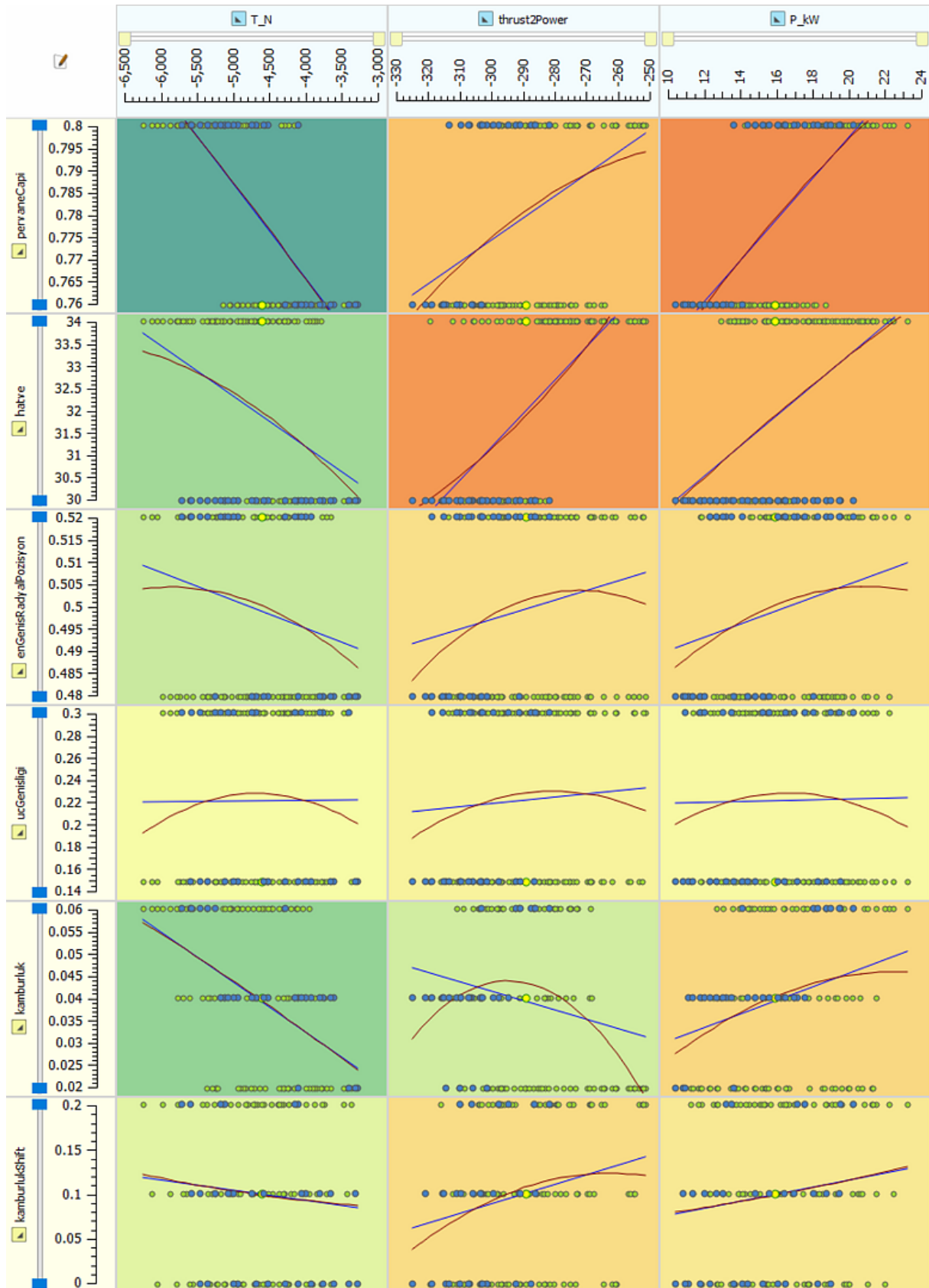


Figure 5.1: The Results of the Sensitivity Analysis in CAESES

6. CONCLUSION AND RECOMMENDATIONS

In this study, the analysis and optimization of axial mixers in biogas plant fermenters were conducted using a Newtonian fluid model. However, it is important to acknowledge that biogas substrates may exhibit non-Newtonian behavior due to their complex composition and rheological properties. Considering non-Newtonian fluid behavior in future studies can provide a more comprehensive understanding of the mixing process and lead to improved design and performance of biogas mixers.

Non-Newtonian fluids exhibit different flow characteristics compared to Newtonian fluids. They can display shear-thinning or shear-thickening behavior, yield stress, and other unique properties that affect the fluid flow patterns and mixing efficiency. By incorporating non-Newtonian fluid models into the analysis, researchers can gain insights into the specific flow behavior of biogas substrates and tailor the mixer design accordingly.

Unique computational fluid dynamics (CFD) models will be developed to be used in the design of axial mixer propellers to operate in biogas plants and non-Newtonian fluids. The energy consumption required for fermenter mixing processes is expected to be reduced by efficient blade design and optimization. Building upon the findings of this study, several future directions and suggestions can be proposed:

Characterization of Biogas Substrates: Conduct a thorough characterization of the rheological properties of biogas substrates to understand their non-Newtonian behavior. This may involve measuring parameters such as viscosity, yield stress, and flow behavior index using rheological tests.

Non-Newtonian Fluid Modeling: Implement non-Newtonian fluid models, such as the power-law model or Herschel-Bulkley model, in computational fluid dynamics (CFD) simulations to accurately capture the flow behavior of biogas substrates. These models can provide a more realistic representation of the fluid dynamics within the biogas plant fermenters.

Design Optimization for Non-Newtonian Fluids: Apply optimization techniques specifically tailored for non-Newtonian fluids to identify optimal blade geometries and operating conditions for improved mixing efficiency. This may involve coupling CFD simulations with optimization algorithms to explore a wider range of design possibilities.

Experimental Validation: Perform experimental studies using non-Newtonian fluids that closely resemble biogas substrates to validate the CFD simulations and assess the performance of the optimized mixer designs. This can involve using rheometers and scaled-up prototypes to measure mixing efficiency and other relevant performance metrics.

Scale-Up Considerations: take into account the potential challenges and considerations associated with scaling up the mixer design and operating conditions for practical implementation in full-scale biogas plant fermenters. This may include considering factors such as power requirements, structural integrity, and maintenance aspects.

Incorporating non-Newtonian fluid behavior into future studies will provide a more accurate representation of the mixing process in biogas plant fermenters. By considering the unique flow characteristics of biogas substrates, researchers can optimize the design of axial mixers to enhance mixing efficiency and ultimately improve the performance of biogas production systems.

REFERENCES

- Belhenniche, S., Aounallah, M., Omar, I., & Çelik, F. (2016). Effect of geometric configurations on hydrodynamic performance assessment of a marine propeller. *Brodogradnja: Teorija i praksa brodogradnje i pomorske tehnike*, 67(4), 31-48.
- Berten, S., Dupont, P., Farhat, M., & Avellan, F. (2007). Rotor-stator interaction induced pressure fluctuations: CFD and hydroacoustic simulations in the stationary components of a multistage centrifugal pump. *In Fluids Engineering Division Summer Meeting* (Vol. 42894, pp. 963-970).
- Błoński, D., Szulc, P., Machalski, A., & Rogula, J. (2021). Numerical simulation and experimental investigation of submersible sewage mixer performance. *In Journal of Physics: Conference Series* (Vol. 1741, No. 1, p. 012007). IOP Publishing.
- Carlton, J. (2018). Marine propellers and propulsion. *Butterworth-Heinemann*.
- Chen, Y. R. (1986). Rheological properties of sieved beef-cattle manure slurry: Rheological model and effects of temperature and solids concentration. *Agricultural wastes*, 15(1), 17-33.
- Doijode, P. S., Hickel, S., van Terwisga, T., & Visser, K. (2022). A machine learning approach for propeller design and optimization: Part I. *Applied Ocean Research*, 124, 103178.
- Doijode, P. S., Hickel, S., van Terwisga, T., & Visser, K. (2022). A machine learning approach for propeller design and optimization: Part II. *Applied Ocean Research*, 124, 103174.
- Gölcü, M., Pancar, Y., & Sekmen, Y. (2006). Energy saving in a deep well pump with splitter blade. *Energy conversion and management*, 47(5), 638-651.
- Gorji, M., Ghassemi, H., & Mohamadi, J. (2019). Effect of rake and skew on the hydrodynamic characteristics and noise level of the marine propeller. *Iranian Journal of Science and Technology, Transactions of Mechanical Engineering*, 43, 75-85.
- Karim, K., Klasson, K. T., Hoffmann, R., Drescher, S. R., DePaoli, D. W., & Al-Dahhan, M. H. (2005). Anaerobic digestion of animal waste: Effect of mixing. *Bioresource technology*, 96(14), 1607-1612.
- Kraume, M. (2003). *Mischen und Rühren: Grundlagen und moderne Verfahren*. Wiley.

- Kress, P., Nägele, H. J., Oechsner, H., & Ruile, S. (2018). Effect of agitation time on nutrient distribution in full-scale CSTR biogas digesters. *Bioresource technology*, 247, 1-6.
- Lemmer, A., Naegele, H. J., & Sondermann, J. (2013). How efficient are agitators in biogas digesters? Determination of the efficiency of submersible motor mixers and incline agitators by measuring nutrient distribution in full-scale agricultural biogas digesters. *Energies*, 6(12), 6255-6273.
- Li, W., Jiang, X., Pang, Q., Zhou, L., & Wang, W. (2016). Numerical simulation and performance analysis of a four-stage centrifugal pump. *Advances in Mechanical Engineering*, 8(10), 1687814016673756.
- Mahmuddin, F. (2017). Rotor blade performance analysis with blade element momentum theory. *Energy Procedia*, 105, 1123-1129.
- Menter, F. (1993, July). Zonal two equation kw turbulence models for aerodynamic flows. In *23rd fluid dynamics, plasmadynamics, and lasers conference* (p. 2906).
- Moeller, G., & Torres, L. G. (1997). Rheological characterization of primary and secondary sludges treated by both aerobic and anaerobic digestion. *Bioresource Technology*, 61(3), 207-211.
- Mola, A., Tezzele, M., Gadalla, M., Valdenazzi, F., Grassi, D., Padovan, R., & Rozza, G. (2019). Efficient reduction in shape parameter space dimension for ship propeller blade design. *arXiv preprint arXiv:1905.09815*.
- Naegele, H. J., Lemmer, A., Oechsner, H., & Jungbluth, T. (2012). Electric energy consumption of the full scale research biogas plant “Unterer Lindenhof”: Results of longterm and full detail measurements. *Energies*, 5(12), 5198-5214.
- Njaastad, E. B., Steen, S., & Egeland, O. (2022). Identification of the geometric design parameters of propeller blades from 3D scanning. *Journal of Marine Science and Technology*, 27(2), 887-906.
- Ohnmacht, B., Lemmer, A., Oechsner, H., & Kress, P. (2021). Demand-oriented biogas production and biogas storage in digestate by flexibly feeding a full-scale biogas plant. *Bioresource Technology*, 332, 125099.
- OpenFOAM Users Guide v10, <https://openfoam.org>

- Rasi, S., Veijanen, A., & Rintala, J. (2007). Trace compounds of biogas from different biogas production plants. *Energy*, 32(8), 1375-1380.
- Reviol, T., Kluck, S., & Böhle, M. (2018). A new design method for propeller mixers agitating non-Newtonian fluid flow. *Chemical Engineering Science*, 190, 320-332.
- Reviol, T., Kluck, S., Etringer, G., Wang, P., & Böhle, M. (2018). Investigation of propeller mixer for agitation of non-Newtonian fluid flow to predict the characteristics within the design process. *Chemical Engineering Science*, 191, 420-435.
- Stel, H., Sirino, T., Ponce, F. J., Chiva, S., & Morales, R. E. M. (2015). Numerical investigation of the flow in a multistage electric submersible pump. *Journal of Petroleum Science and Engineering*, 136, 41-54.
- World Energy Outlook 2019. Available online: <https://www.iea.org/reports/world-energy-outlook-2019>. (accessed on 15 March 2023) .
- Yin, C., Rosenvinge, C. K., Sandland, M. P., Ehlers, A., & Shin, K. W. (2023). Improve Ship Propeller Efficiency via Optimum Design of Propeller Boss Cap Fins. *Energies*, 16(3), 1247.
- Zhou, L., Shi, W., Lu, W., Hu, B., & Wu, S. (2012). Numerical investigations and performance experiments of a deep-well centrifugal pump with different diffusers.
- Zhou, L., Shi, W., & Wu, S. (2013). Performance optimization in a centrifugal pump impeller by orthogonal experiment and numerical simulation. *Advances in Mechanical Engineering*, 5, 385809.
- Zlokarnik, M. R. (1999). *Theorie und Praxis*.

APPENDIX

Velocity Boundary Conditions

```
FoamFile
{
  version 2.0;
  format binary;
  class volVectorField;
  arch "LSB;label=32;scalar=64";
  location "0";
  object U;
}
// ***** //
dimensions [0 1 -1 0 0 0];
internalField uniform (0 0 0.1);
boundaryField
{
  farField
  {
    type noSlip;
  }
  inlet
  {
    type pressureInletOutletVelocity;
    value uniform (0 0 0.1);
  }
  outlet
  {
    type inletOutlet;
    inletValue uniform (0 0 0);
    value uniform (0 0 0);
  }
  propeller
  {
    type noSlip;
  }
  AMI_rotor
  {
    type cyclicAMI;
    value nonuniform List<vector>
  }
  AMI_stator
  {
    type cyclicAMI;
    value nonuniform List<vect
  }
}
// ***** //
```

Pressure Boundary Conditions

```
FoamFile
{
  version 2.0;
  format binary;
  class volScalarField;
  arch "LSB;label=32;scalar=64";
  location "0";
  object p;
}
// ***** //
dimensions [0 2 -2 0 0 0];
internalField uniform 0;
boundaryField
{
  farField
  {
    type zeroGradient;
  }
  inlet
  {
    type totalPressure;
    rho rho;
    psi none;
    gamma 1;
    p0 uniform 0;
    value uniform 0;
  }
  outlet
  {
    type fixedValue;
    value uniform -0.001;
  }
  propeller
  {
    type zeroGradient;
  }
  AMI_rotor
  {
    type cyclicAMI;
    value uniform 0;
  }
  AMI_stator
  {
    type cyclicAMI;
    value uniform 0;
  }
}
// ***** //
```

Boundary Conditions for Turbulent Kinetic Energy

```
FoamFile
{
  version 2.0;
  format binary;
  class volScalarField;
  arch "LSB;label=32;scalar=64";
  location "0";
  object k;
}
// ***** //
dimensions [0 2 -2 0 0 0];
internalField uniform 1e-09;
boundaryField
{
  farField
  {
    type kqRWallFunction;
    value uniform 1e-09;
  }
  inlet
  {
    type fixedValue;
    value uniform 1e-09;
  }
  outlet
  {
    type inletOutlet;
    inletValue uniform 1e-09;
    value uniform 1e-09;
  }
  propeller
  {
    type kqRWallFunction;
    value uniform 1e-09;
  }
  AMI_rotor
  {
    type cyclicAMI;
    value nonuniform List<scalar>
  }
  AMI_stator
  {
    type cyclicAMI;
    value nonuniform List<scalar>
  }
}
// ***** //
```

Boundary Conditions for Omega

```
FoamFile
{
  version 2.0;
  format binary;
  class volScalarField;
  arch "LSB;label=32;scalar=64";
  location "0";
  object omega;
}
// ***** //
dimensions [0 0 -1 0 0 0];
internalField uniform 0.05;
boundaryField
{
  farField
  {
    type omegaWallFunction;
    value uniform 0.05;
  }
  inlet
  {
    type fixedValue;
    value uniform 0.05;
  }
  outlet
  {
    type inletOutlet;
    inletValue uniform 0.05;
    value uniform 0.05;
  }
  propeller
  {
    type omegaWallFunction;
    value uniform 0.05;
  }
  AMI_rotor
  {
    type cyclicAMI;
    value nonuniform List<scalar>
  }
  AMI_stator
  {
    type cyclicAMI;
    value nonuniform List<scalar>
  }
}
// ***** //
```

Turbulent Viscosity Boundary Conditions

```
FoamFile
{
  version 2.0;
  format binary;
  class volScalarField;
  arch "LSB;label=32;scalar=64";
  location "0";
  object nut;
}
// ***** //
dimensions [0 2 -1 0 0 0];
internalField uniform 0;
boundaryField
{
  farField
  {
    type nutUSpaldingWallFunction;
    value uniform 0;
  }
  inlet
  {
    type calculated;
    value uniform 0;
  }
  outlet
  {
    type calculated;
    value uniform 0;
  }
  propeller
  {
    type nutUSpaldingWallFunction;
    value uniform 0;
  }
  AMI_rotor
  {
    type cyclicAMI;
    value uniform 0;
  }
  AMI_stator
  {
    type cyclicAMI;
    value uniform 0;
  }
}
// ***** //
```

T.C.

**AYDIN ADNAN MENDERES UNIVERSITY
GRADUATE SCHOOL OF NATURAL AND APPLIED SCIENCES**

SCIENTIFIC ETHICAL STATEMENT

I hereby declare that I composed all the information in my master's thesis entitled "DESIGN AND OPTIMIZATION OF PROPELLER OF SUBMERSIBLE MIXER FOR BIOGAS PLANTS" within the framework of ethical behaviour and academic rules, and that due references were provided and for all kinds of statements and information that do not belong to me in this study in accordance with the guide for writing the thesis. I declare that I accept all kinds of legal consequences when the opposite of what I have stated is revealed.

UTKU KÖSE

03/08/2023

CIRRICULUM VITAE

Last name, First name : Köse, Utku

Education

Level	Institute	Date of graduation
M.Sc. - Mechanical Engineering	Adnan Menderes University	Cont.
B.Sc. – Mechanical Engineering	Pamukkale University	September 2009

WORK EXPERIENCE

Year	Place/ Institute	Title
2009-2010	Frekans Makina	Design Engineer
2011-2014	EYS Endüstri Makine San.	R&D Engineer
2014-Con	EYS Endüstri Makine San.	R&D Manager

ACADEMIC PUBLICATIONS

1. ARTICLES

Surface Topological Investigation of Seal Bushing by Using Chromium Plating Process

Proceedings of the 12th International Conference on Measurement and Quality Control - Cyber Physical Issue (in Belgrade, SERBIA) Proceedings of the 12th International Conference on Measurement and Quality Control - Cyber Physical Issue (in Belgrade, SERBIA)

Springer Nature · 21 May 2019Springer Nature · 21 May 2019

Comparison of Prototyping Costs Between Additive and Classical Manufacturing Techniques
4th INTERNATIONAL CONGRESS ON 3D PRINTING (ADDITIVE MANUFACTURING)
TECHNOLOGIES AND DIGITAL INDUSTRY 2019

11 - 14 APRIL, 2019, ANTALYA, TR

Design and Development of Drum Granulator

International Symposium for Production Research 2020

2. PROJECTS

“Self Propelled Compost Mixing Machine”

Deputy Project Manager

Project No: 7140908

15.08.2014/25.05.2016

“Mobile Shredder Design”

Project No: 3170680

Project Manager

26.10.2017/28.11.2019

“Design and Development of a Highly Efficient Axial Mixer Using High Performance
Calculation Methods for Use in Biogas and Water Treatment Facilities”

Project No: 3192298

Project Manager

09.04.2020/15.06.2023

“Submersible Type Fertilizer/Wastewater Pump Development Using High Performance
Computing Methods”

Project No: 3220850

Project Manager

13.03.2023/ Devam Ediyor